RSC Advances

PAPER

View Article Online
View Journal | View Issue

Cite this: *RSC Adv.*, 2025, **15**, 5042

Simultaneous adsorption of sulfamethoxazole and neodymium from wastewater by a MXene-, α-aminophosphonate-, and sulfated fucan-based ternary composite based on anion-synergistic interactions†

Irfan Ijaz, *[a] Aysha Bukhari,*[a] Ammara Nazir,[a] Ezaz Gilani,[a] Hina Zain,[b] Attia Shaheen,[c] Mohammed Rafi Shaik,[d] Mujeeb Khan[d] and Jilani P. Shaik[e]

The simultaneous removal of antibiotics and heavy metal ions is of utmost importance because of their hazardous effects on the environment and humans. For the adsorption of sulfamethoxazole (SMX) and neodymium (Nd^{3+}) in mono- and binary contaminant systems (SMX–Nd^{3+} and Nd^{3+}–SMX), a novel composite was designed using sulfated fucan (**FuS**), **MXene**s, and α-aminophosphonates (**AMP**s) in this study. As far as we know, the concurrent adsorption of SMX and Nd^{3+} employing materials made of **MXene**s, **FuS**, and **AMP**s with this specific structure has not yet been reported. At 318 K, the **FuS@MXene@AMP** adsorbent demonstrated excellent adsorption capacities of 448.91 and 255.78 mg g^{-1} for SMX and Nd^{3+}, respectively. The pseudo-first-order (PSO) kinetic model was the most appropriate for depicting the adsorption of SMX and Nd^{3+} among all the tested kinetic models. The adsorption of SMX and Nd^{3+} is better described by the Langmuir isotherm model with a higher value of adsorption capacity and R^2. The simultaneous presence of Nd^{3+} and SMX promoted mutual sorption between the antibiotic and metal ions in the binary systems. The results of FTIR and XPS studies indicated that the removal mechanisms were primarily due to hydrogen bonding, complexation, electrostatic interaction, and π–π interaction.

Received 14th December 2024
Accepted 30th January 2025

DOI: 10.1039/d4ra08766f

rsc.li/rsc-advances

1 Introduction

Neodymium ions (Nd^{3+}) and antibiotics are commonly used in diagnosis and treatment, and they eventually coexist in hospital wastewater.[1,2] On the one hand, Nd^{3+} contamination of the environment has hazardous impacts on terrestrial and aquatic ecosystems.[3] On the other hand, Nd^{3+} is one of the five most important and strategic rare earth elements (REEs) and has been extensively employed in designing cutting-edge and clean energy technologies, such as permanent magnets,[4] laser generators,[5] and electronic devices.[6] However, the steady supply of neodymium has been restricted, making it a hot topic. This is because of limited mineral reserves,[7] growing global needs,[8] and tight export restrictions from various Nd-producing countries.[9] Consequently, recycling and recovering Nd^{3+} from hospital waste and industrial wastes that contain Nd^{3+}, such as red mud, coal fly ash, phosphogypsum, and mine wastewater, are considered an environmentally sound approach to address the Nd^{3+} supply crisis and lessen the impact on the environment. Because residual SMX encourages the growth of antibiotic-resistant bacteria and the spread of antibiotic resistance genes, it presents a significant risk to human health, much like other antibiotic residues. Neodymium is present in some electronic equipment used extensively in hospitals (*e.g.*, in hard drives, medical imaging equipment, or other electronic components). Hospital e-waste may contain Nd^{3+} and SMX if it is disposed improperly. Similarly, hospital effluents consisting of SMX may get mixed with industrial and municipal effluents that incorporate Nd^{3+} from different sources (such as manufacturing processes or electronics), which makes removal more challenging. When Nd^{3+} is reacted with SMX, its chemical characteristics change and its toxicity rises. Therefore, the concurrency of Nd^{3+} and SMX may improve the generation and spread of antibiotic resistance to a greater extent. Consequently, developing a practical strategy for the individual and

[a]*School of Chemistry, Faculty of Basic Sciences and Mathematics, Minhaj University Lahore, Lahore 54700, Pakistan. E-mail: iffichemixt266@gmail.com; ayshabukhari.che@mul.edu.pk*

[b]*Department of Chemistry, University of Cincinnati, OH 45221, USA*

[c]*Institute for Advanced Study, Shenzhen University, Shenzhen, Guangdong, P. R. China*

[d]*Department of Chemistry, College of Science, King Saud University, P. O. Box 2455, Riyadh 11451, Saudi Arabia*

[e]*Department of Biochemistry, College of Science, King Saud University, P. O. Box 2455, Riyadh 11451, Saudi Arabia*

† Electronic supplementary information (ESI) available. See DOI: https://doi.org/10.1039/d4ra08766f

simultaneous adsorption of SMX and Nd^{3+} from hospital effluents is essential.

Different wastewater remediation approaches, like membrane filtration,[10] photocatalysis,[11] advanced oxidation processes,[12] biodegradation, ion exchange,[13] electrochemical degradation,[14,15] and adsorption,[16,17] have been utilized to eliminate Nd^{3+} and SMX from wastewater. Adsorption techniques have drawn significant attention because of their adaptability in terms of cost-effectiveness,[18] material sources,[19,20] high efficiency,[21] absence of by-products,[22] quick adsorption rates,[23] and ease of operation,[24] making them perfect for eliminating SMX and Nd^{3+} contamination.

Natural polysaccharide biopolymers have been derived from different natural sources and have attained notable attention as adsorbents in contaminant elimination because of their biodegradability,[25] affordability,[26] and renewable nature.[27,28] Sulfated fucan is a natural polysaccharide primarily comprised of fucose.[29] Egg jellies, sea cucumbers, sea urchins, and brown algae are the primary natural sources of sulfated fucan.[30] Sulfated fucan is widely employed in the pharmaceutical industries, food, and therapeutic agents because of its outstanding biological activities, such as immunoregulatory,[31,32] antitumor,[33] anti-inflammatory,[34] antiviral,[35] antioxidant,[29] anticoagulant,[36,37] and antithrombotic properties.[38] Sulfated fucan contains various moieties, such as hydroxyl, oxygen, and sulfate groups, which aid in drug binding through hydrogen bonding, complexation, and electrostatic interaction. Despite this, sulfated fucan exhibits lower adsorption capacity in the adsorption of antibiotics and Nd^{3+}. The adsorption capability of natural polysaccharides have been enhanced by physical and chemical modifications.[39–42]

MXene, a novel two-dimensional (2D) material, has attracted notable interest because of its physicochemical stability,[43] outstanding conductivity,[43] distinctive laminated structure,[44] and ample surface functionalities.[45] Its applications include energy conversion, bioactive materials, and catalysis.[46] Typically, **MXene** is written as $M_{n+1}X_nT_x$ ($n = 1, 2, 3$), where T_x is the surface group (–O, –F, and –OH), M is the transition metal element, and X stands for C or/and N. Furthermore, because of its higher surface area, hydrophilic character, abundant active functional groups, and ability to offer numerous sites for direct adsorption and ion exchange of heavy metals[47] and dyes, **MXene** has been studied as an effective adsorbent for water treatment.[48,49] Adil *et al.* prepared a Cu/Ni-**MXene** composite with an adsorption capacity of 66.30 mg g^{-1} for the removal of Cr.[50] With an adsorption capacity of 208.20 mg g^{-1}, Ghani *et al.* prepared sodium intercalated $Ti_3C_2T_x$ **MXene** for the adsorption of ciprofloxacin.[51] **MXene** still encounters multiple issues, such as inadequate renderability, expensive, and aggregation and oxidation, which could decrease its reactivity with contaminants.

Organophosphorus molecules, like α-aminophosphonates, structurally resemble amino acids since they substitute the carboxylic group with a phosphonic acid or similar moiety. This resemblance may demonstrate their elevated reactivity with pollutants and multiple applications. Research on uranium adsorption employing trialkylphosphine oxides and tributyl phosphate indicated that the P=O functional group demonstrated an efficient coordination bond with U(VI). To the best of our knowledge, however, there have been no reports on the concurrent adsorption of SMX and Nd^{3+} using sulfated fucan, **MXene**, and α-aminophosphonates.

In the current analysis, we have prepared α-aminophosphonates and **MXene**-functionalized sulfated fucan (**FuS@MXene@AMP**) composite by incorporating sulfated fucan, **MXene**, and α-aminophosphonates. The composite development philosophy in the current research revolves around maximizing the synergistic impacts of integrating sulfated fucan, **MXene**, and α-aminophosphonates to prepare a novel adsorbent material with improved adsorption capabilities for wastewater treatment. The introduction of α-aminophosphonates and **MXene** modifications efficiently introduced phosphonate, oxygen, carboxymethyl moieties, fluorine, hydroxyl, amino, and thiocarbonyl groups into sulfated fucan, which increase the density of the active sites for the adsorption of SMX and Nd^{3+} mono-pollutant system and binary pollutant system through hydrogen bonding, complexation, electrostatic interaction, and π–π interaction. The compositional, morphological, and structural characteristics of the **FuS@MXene@AMP** composites have been systematically studied utilizing FTIR, SEM, XPS, and BET analyses. Under distinct solution environments, such as temperature, pH, temperature, and concentration, the sorption performance of SMX and Nd^{3+} by the **FuS@MXene@AMP** adsorbent has been studied. The sorption characteristics have been determined by employing thermodynamic, isothermal, and kinetic models. Furthermore, employing FTIR and XPS analyses, the possible adsorption mechanism for SMX, Nd^{3+}, and SMX + Nd^{3+} by the **FuS@MXene@AMP** adsorbent has been revealed. These results highlight a versatile approach for designing **FuS**-based composites with outstanding adsorption capability appropriate for real-world wastewater remediation.

2 Experimental section

2.1. Materials

Thiocarbazide, *p*-phthalaldehyde, and triphenylphosphite were provided by Shanghai Chemical Reagent Co., Ltd. Acetonitrile (CH_3CN), titanium (Ti) powder, aluminum (Al) powder, copper(II) triflate (Cu $(TOF)_2$), and acetone were supplied by Shanghai Aladdin Biochemical Technology Co., Ltd. Hydrofluoric acid (HF), hydrochloric acid (HCL), neodymium ions (Nd^{3+}), and sulfamethoxazole were provided by Sigma-Aldrich.

2.2. Synthesis of the Ti_3AlC_2 MAX phase

The detailed process for the synthesis of the Ti_3AlC_2 MAX phase is provided in Text S1.†

2.3. Preparation of MXene

The strategy employed for the **MXene** preparation was based on the method reported by Chen *et al.*.[52] Briefly, 5 g of HF was added to 50 mL of HCl solution and stirred for 10 min. After 15 minutes of mixing 37 g of the MAX phase (Ti_3AlC_2) in 30 mL of HCl, the mixture was gradually added to the HF/HCL solution

while being constantly stirred. Subsequently, the resultant product underwent a 15 hours reaction with continuous magnetic stirring at 60 °C. A dark-colored suspension was produced by centrifuging the obtained suspension at 1500 rpm after cleaning with deionized water.

2.4. Preparation of sulfated fucans

According to an earlier published analysis, the body wall of sea cucumbers was used to isolate sulfated fucans (**FuS**). The dried body walls of sea cucumbers were ground and then incubated with papain. By precipitating enzymatic hydrolysate with 80% ethanol, **FuS** was produced, which was subsequently purified employing gel exclusion chromatography.[53]

2.5. Synthesis of α-aminophosphonate materials

α-Aminophosphonates were prepared using the procedures reported by Imam *et al.* Fig. S1† exhibits the proposed structures of the material and its preparation pathway. Thiocarbazide,

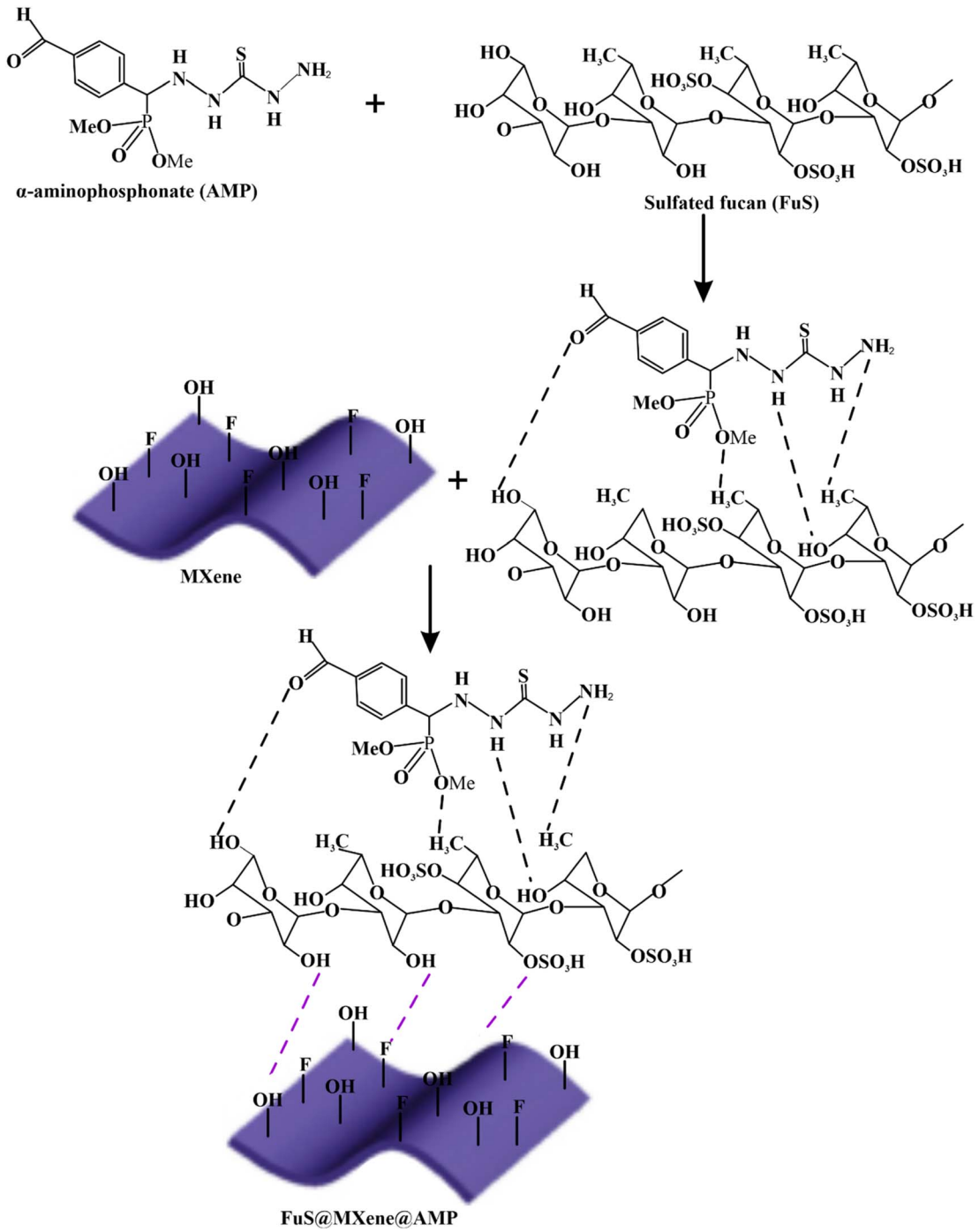

Scheme 1 The mechanism for the preparation of the FuS@MXene@AMP composite.

triphenylphosphite, and *p*-phthalaldehyde, with different molar ratios of 1 : 1 : 1 were mixed in 5 mL of acetonitrile (CH_3CN) for designing **AMP**. The resultant solution was agitated for 15 min at room temperature. Next, a Lewis acid catalyst, copper(II) triflate (Cu $(TOF)_2$), was immediately introduced into the above solution at a 20% (w/w) concentration. The resultant solution was filtered, cleaned with acetonitrile, and dried in air to yield α-aminophosphonate after stirring for 72 h at room temperature.

2.6. Synthesis of FuS@MXene@AMP composite

0.5 g of **FuS** and 1.3 g of α-aminophosphonates were introduced to a 6 mL **MXene** suspension to produce the **FuS@MXene@AMP** composite. The resultant solution produced a gelatinous substance after being centrifuged for 25 minutes at 3500 rpm and ultrasonically dispersed for 65 minutes. The gelatinous substance was transferred to a vacuum oven and heated for 18 hours at 70 °C to get the **FuS@MXene@AMP** composite. After being crushed into powder, the synthesized **FuS@MXene@AMP** composite was cleaned with acetone and dried for 6 hours at 55 °C. Scheme 1 depicts the mechanism for the preparation of the **FuS@MXene@AMP** composite.

2.7. Characterizations

The functional groups of the ternary composite were determined by employing a Fourier transform infrared spectrometer (FT-IR; Nicolet NEXUS 670). X-ray photoelectron spectroscopy (XPS; PHI 5000, ULVAC-PHI, Japan) was used to analyze the adsorbent chemical states. Brunauer–Emmett–Teller (BET; ASAP 2050, America) was employed to investigate the pore size distribution and surface area of the ternary composites. Using a scanning electron microscope (SEM, FEI TF20, USA), the morphologies of the ternary adsorbent were examined.

2.8. Batch sorption studies

The batch adsorption study is discussed in detail in Text S2.†

2.9. Extraction process

The extraction process is discussed in detail in Text S3.†

3 Result and discussion

3.1. Characterization of the FuS@MXene@AMP composite

Fig. 1(a) displays the FTIR spectra of the synthesized **FuS**, **FuS@MXene**, and **FuS@MXene@AMP** composite. The stretching vibration of S=O at 1237 cm^{-1} is attributed to the **FuS** peaks in the FTIR spectrum. For **FuS**, the C–O–C stretching vibration of the pyran ring was observed at 1025 cm^{-1}. The peak at 3428 cm^{-1} corresponds to the OH group of **FuS**. In the FTIR spectrum of **FuS@MXene**, three new peaks appeared at 623, 1119, and 1645 cm^{-1}, corresponding to the Ti–O, C–F, and C=O groups of **MXene**. Xing *et al.* have reported similar peaks for **MXene**.[54] In contrast to **FuS@MXene**, a new peak at 1619 cm^{-1} corresponding to the primary and secondary –NH groups appeared in the FTIR spectrum of **FuS@MXene@AMP**. Additionally, a peak at 2830 cm^{-1} verified the existence of aromatic and aliphatic C–H groups in the prepared **FuS@MXene@AMP** ternary composite. Peaks at 1275 cm^{-1} are associated with the P=O groups. Imam *et al.* have reported similar peaks for α-aminophosphonate.[55] The appearance of NH, C–H, and P=O groups justified the successful introduction of α-aminophosphonate in **FuS@MXene**. The FTIR peaks confirmed the presence of Ti–O, C=C, C–F, $HOSO_3^-$, P=O, NH, and OH groups, which increased the adsorption performance of the adsorbent. SMX and Nd^{3+} adsorbed on the surface of the adsorbent through hydrogen bonding, π–π interaction, and electrostatic interaction between Ti–O, C=C, C–F, $HOSO_3^-$, P=O, NH, and OH groups of the adsorbent and SMX and Nd^{3+}.

The XPS survey spectra for the **FuS**, **FuS@MXene**, and **FuS@MXene@AMP** composites are depicted in Fig. 1(b). In the **FuS** XPS spectrum, typical XPS signals of S 2p, S 2s, C 1s, and O 1s were detected. In contrast to **FuS**, two new XPS signals of Ti 2p and F 1s appeared in the XPS spectrum of **FuS@MXene**. The appearance of Ti 2p and F 1s XPS signals suggested the

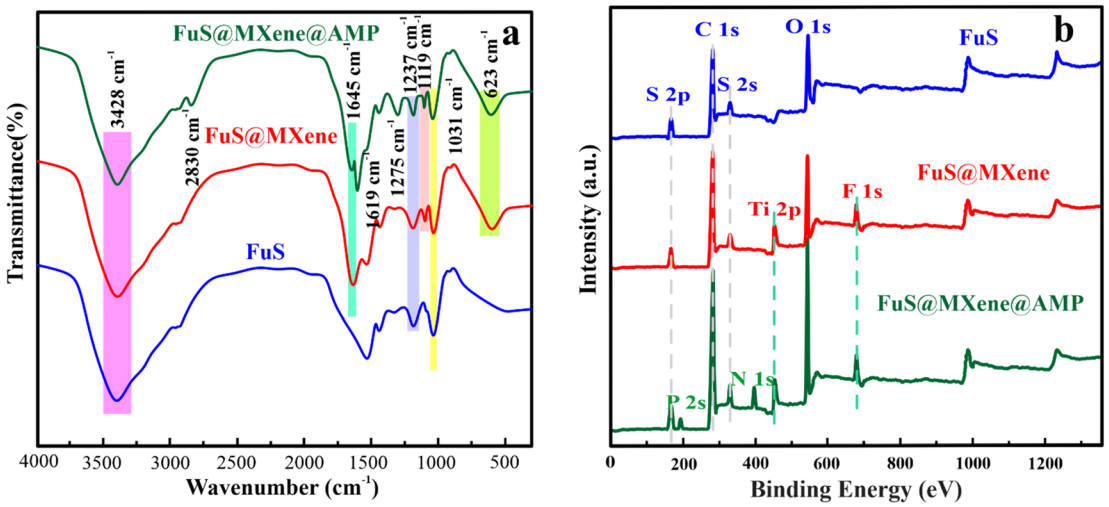

Fig. 1 FTIR spectra (a) and XPS (b) spectra of FuS, FuS@MXene, and the FuS@MXene@AMP composite.

successful introduction of **MXene** in **FuS**. In the XPS survey spectra of **FuS@MXene@AMP**, two XPS peaks of P 2p and N 1s emerged. The appearance of new XPS peaks of P 2p and N 1s and the increased intensities of O 1s, S 2s, S 2p, and C 1s justified the successful preparation of the ternary composite.

Fig. 2 displays the high-resolution XPS spectra of these elements. In the high-resolution XPS C 1s survey spectrum, C–H and C–C functional groups appeared at a binding energy of 284.28 eV. Similarly, at a binding energy of 284.28 eV, the C–S, C–OH, and C–P groups emerged. C=O, C–O–P, and C–O–C groups were observed at a binding energy of 287.20 eV in the C 1s XPS spectrum (Fig. 2(a)).[56,57] The characteristic XPS signals of OH, C=O, P–O, and P–O–C were detected at 530.51, 532.31, and 532.94 eV, respectively, according to the O 1s XPS spectrum displayed in Fig. 2(b).[58,59] For N 1s, two groups appeared at a binding energy of 399.57 and 401.92 eV, attributing to NH_2, NH and NH^{2+}, NH^{3+} groups, respectively.[60] Three sulfur-containing groups corresponding to C–S, C=S, and S–O ($2p_{3/2}$) groups emerged in the case of S 2p at binding energies of 161.23, 163.54, and 166.81 eV. XPS signals relating to C–S, C–OH, C–H, C–C, C–P, OH, C=O, P–O, P–O–C, NH_2, NH, and $HOSO_3^-$ groups of adsorbents are observed, which offered active sites for the adsorption of SMX and Nd^{3+}.

The BET-specific surface area (SSA) and pore size distribution for the **FuS**, **FuS@MXene**, and **FuS@MXene@AMP** composite are depicted in Fig. 3(a and b). **MXene** indicates characteristic microporous properties, as seen in Fig. 3(a). The **FuS@MXene** and **FuS@MXene@AMP** composite indicated type IV nitrogen adsorption/desorption isotherms with characteristic H_3 hysteresis loops, suggesting the existence of mesopores and micropores. The specific surface area of the **FuS@MXene@AMP** composite was 428 $m^2\ g^{-1}$, which was significantly greater than that of **FuS@MXene** (341 $m^2\ g^{-1}$) and **FuS** (147 $m^2\ g^{-1}$), as exhibited in Fig. 3(a). The higher surface area of the **FuS@MXene@AMP** composite was attributed to the presence of pores and lamellar morphology.[61,62] According to Fig. 3(b), **FuS** exhibited pore diameters ranging from 2 to 119 nm, averaging 21.8 nm (4 V/A by BET). **FuS@MXene** and **FuS@MXene@AMP** composite had average pore diameters of 19.4 and 18.5 nm, respectively, less than that of **FuS**. The **FuS@MXene@AMP** composite is more promising than **FuS@MXene** and **FuS** in forming mesoporous structures, which is advantageous for adsorption.[63] This enhanced BET surface area and pore diameters of the **FuS@MXene@AMP** adsorbent than **FuS** and **FuS@MXene** are anticipated to promote the diffusion of SMX and Nd^{3+} during the adsorption of pollutants, enabling faster and more efficient adsorption of SMX and Nd^{3+}.

The morphologies of **FuS**, **FuS@MXene**, and **FuS@MXene@AMP** are studied employing SEM, as depicted in Fig. 4(a–e). The Al layers are successfully etched from the MAX phase (Ti_3AlC_2), as evidenced by the accordion-like multilayer morphology (Fig. 4(a)). Fig. 4(b) indicates small-sized particles of **FuS** with irregular shapes. Large, irregularly shaped **AMP** particles are visible in Fig. 4(c). The layered structure of **MXene**, larger **AMP**

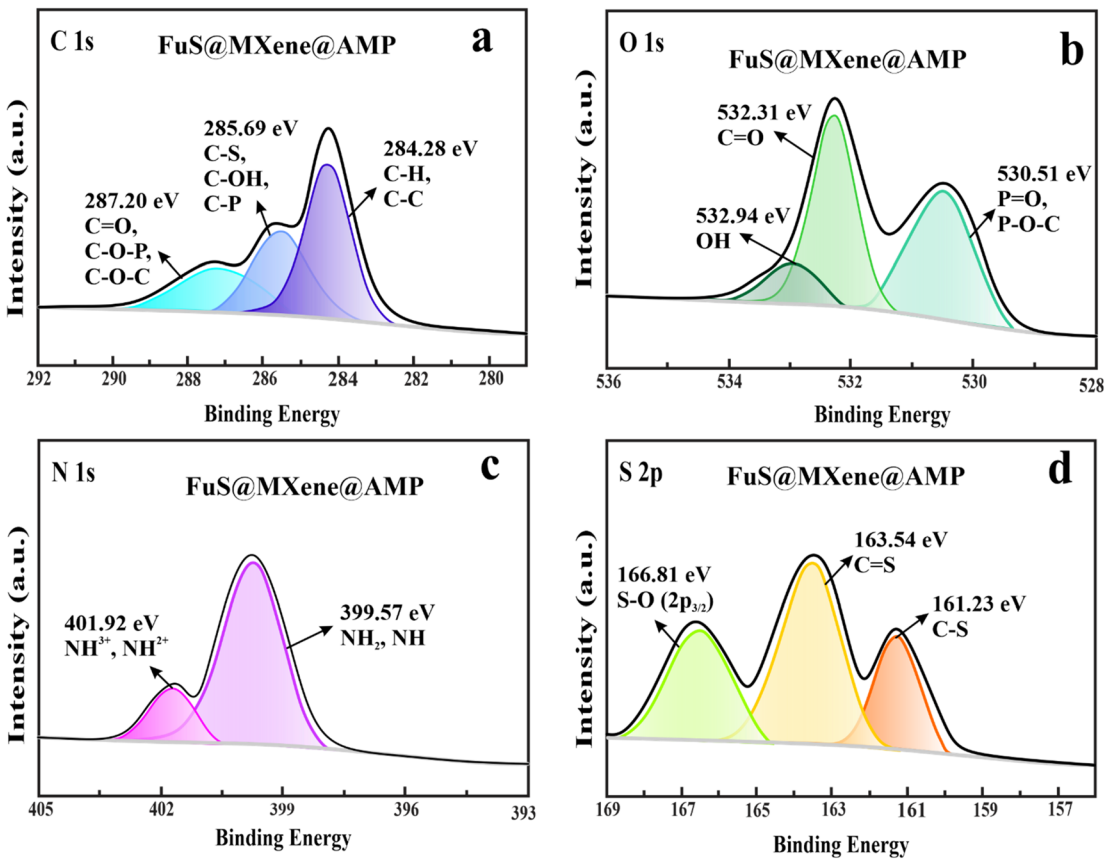

Fig. 2 High-resolution XPS spectra of the **FuS@MXene@AMP** composite before adsorption of SMX and Nd^{3+}: C 1s (a), O 1s (b), N 1s (c), and S 2p (d).

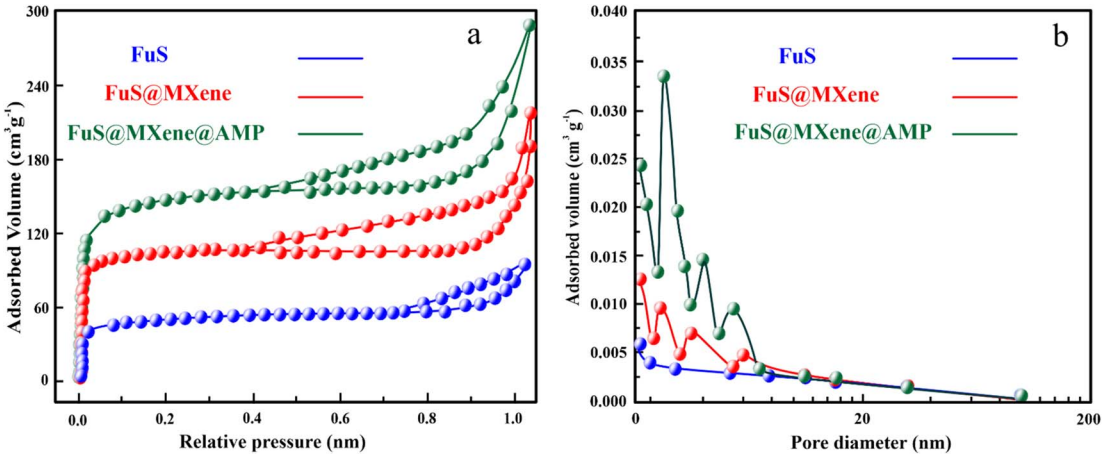

Fig. 3 N_2 adsorption–desorption (a) and pore distribution (b) of **FuS**, **FuS@MXene**, and the **FuS@MXene@AMP** composite.

particles, and tiny **FuS** particles are all visible in Fig. 4(d and e), which confirms the successful formation of the **FuS@MXene@AMP** composite. Fig. 4(e) depicts the porous surface of the composite, which is appropriate for the adsorption of Nd^{3+} and SMX.

3.2. Adsorption of SMX and Nd^{3+} by FuS@MXene@AMP composite in mono-pollutant systems

3.2.1. Effect of pH. Because pH can alter the speciation of adsorbates in the solution and affect the surface charge of the adsorbent, the adsorption process considers pH one of the most significant parameters.[64] Batch adsorption experiments were performed employing solutions with different pH values to examine the influence of pH on the adsorption of SMX and Nd^{3+}. The amine functional groups in the sulfamethoxazole antibiotic have two pK_a values of 1.67 and 5.7.[65] Specifically, SMX is presented in three distinct forms: cationic state (SMX^+) at pH < 1.67, zwitterionic form, also called the neutral state (SMX^0) at 1.67 < pH < 5.7, and anionic state (SMX^-) at pH > 5.7.[66] **FuS@MXene@AMP** had a point of zero charges (pH_{pzc}) of

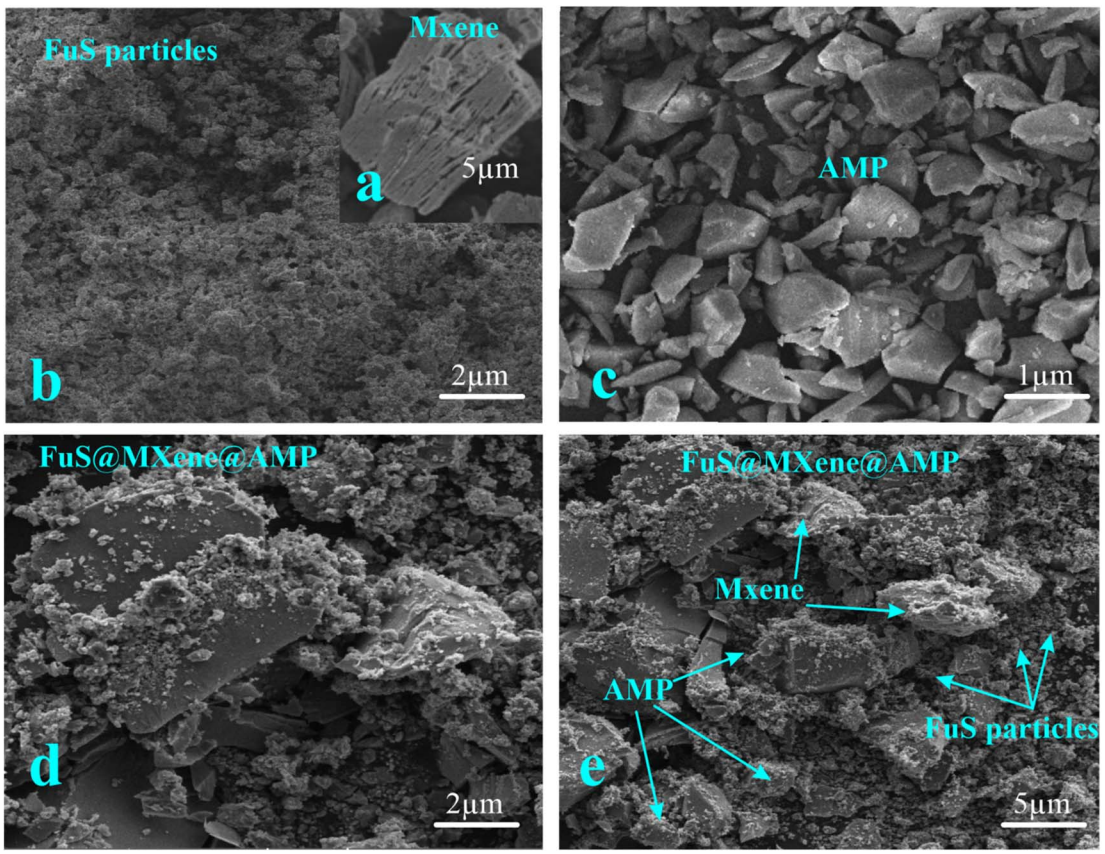

Fig. 4 SEM images of the **MXene** (a), **FuS** (b), **AMP** (c), and **FuS@MXene@AMP** (d and e) composite.

approximately 3.0, as exhibited in Fig. S2.† The **FuS@MXene@AMP** surface had a negative charge when the pH was higher than 3.0. At a pH value below 1.67, the adsorption capacity of the **FuS@MXene@AMP** adsorbent for SMX was negligible due to the strong electrostatic repulsion between the positively charged adsorbents and the cationic SMX^{+}. When the pH value was raised from 1.67 to 5.7, the **FuS@MXene@AMP** adsorbent's capacity for SMX increased, suggesting that maximum adsorption of SMX by the **FuS@MXene@AMP** adsorbent occurred in the zwitterionic form. The maximum removal rate of SMX was observed at a pH value of 5, as illustrated in Fig. 5. The primary cause of the higher sorption capability and removal rate (%) in the zwitterionic or neutral state of SMX was the hydrogen bonding between the F, OH, P=O, NH, and $HOSO_3^{-}$ groups of the **FuS@MXene@AMP** adsorbent and the S=O and NH groups of SMX. Apart from hydrogen bonding, there were also π–π interactions between the benzene ring in the **FuS@MXene@AMP** adsorbent and the SMX. In this work, hydrogen bonding and π–π interaction are the dominating interactions that played a vital role in the adsorption of SMX by the adsorbent. Xue *et al.* have reported similar interactions in the adsorption of SMX.[67] When the pH value was raised from 5.7 to 10, the **FuS@MXene@AMP** adsorbent's adsorption capacity for SMX was lowered gradually due to the quick conversion of the zwitterionic form (SMX^{0}) to an anionic (SMX^{-}) form. The anionic **FuS@MXene@AMP** composite and negatively charged (SMX^{-}) exhibited electrostatic repulsion, significantly hindering SMX's adsorption onto the adsorbent. Because of π–π interactions and hydrogen bonding, SMX^{-} could still adsorb on the negatively charged **FuS@MXene@AMP** surface despite this strong electrostatic repulsion.

The influence of pH on Nd^{3+} sorption by TCFs was studied at pH values ranging from 1 to 7 due to the precipitation of REE at pH values above 7.[68] Fig. 5(b) illustrates the adsorption of Nd^{3+} by the adsorbent as a function of pH. When the pH was below 3.0 (pHPZC), the **FuS@MXene@AMP** surface had a positive charge, and the adsorption of Nd^{3+} by the adsorbent was negligible due to the strong electrostatic repulsion between the positively charged **FuS@MXene@AMP** surface and Nd^{3+} as well as the inhabitation impact of –OH deprotonation. When the pH of the solution slowly increases to 5.0, the positively charged **FuS@MXene@AMP** transformed into negatively charged, and the adsorption capacity or removal rate of the adsorbent for Nd^{3+} was improved due to electrostatic interaction between the negatively charged **FuS@MXene@AMP** adsorbent and positively charged Nd^{3+}, and more OH species may be deprotonated. The hydrolysis of Nd^{3+} at higher pH values of 6 and 7 may be the primary cause of the slight drop in adsorption capacity.[69,70]

3.2.2. Effect of coexisting ions, adsorption selectivity, and type of adsorbent. Various inorganic and organic elements exist in wastewater that can affect the adsorption of SMX and Nd^{3+}. The influence of ionic strength on adsorption capacity was studied by changing the concentration of $CaCl_2$ in the SMX or Nd^{3+} solutions. Variations in $CaCl_2$ concentration slightly affect the removal rate and sorption capabilities of SMX and Nd^{3+}, as shown in Fig. 6(a and b). This implies that $CaCl_2$ slightly influences the removal ability of **FuS@MXene**@AM. Specifically, the sorption of Nd^{3+} may be influenced by other cations, including Na^{+}, Ca^{2+}, Mg^{2+}, and Al^{3+}, present in the wastewater. The influence of varying Na^{+}, Ca^{2+}, Mg^{2+}, and Al^{3+} on the removal rate and sorption capability of Nd^{3+} was examined, as illustrated in Fig. S3.† The adsorption capability and removal rate of Nd^{3+} were negligibly affected by the presence of K^{+}. Moreover, Al^{3+}, Mg^{2+}, and Ca^{2+} coexistence significantly declined Nd^{3+}'s adsorption capabilities because they competed with Nd^{3+} for sorption sites. 90% of the Nd^{3+} can still be adsorbed efficiently. Additionally, when the concentration of humic acid (HA) increased from 0 to 20 mg L^{-1}, the adsorption capacities of SMX by the composite improved and then declined. Due primarily to competition for adsorption sites, HA hampered the sorption of SMX at higher humic acid concentrations. 90% of the SMX was still adsorbed efficiently in the presence of HA, as exhibited in Fig. 6(c). The better humic acid resistance of the adsorbent demonstrated competitive adsorption, which occurred mainly on the nitrogen- and oxygen-compromising **MXene**, sulfated fucan, and α-aminophosphonate composites as the adsorption sites because of the relatively better affinity of humic acid to these nitrogen- and oxygen-compromising groups of nitrogen- and oxygen-compromising **MXene**, sulfated fucan, and α-

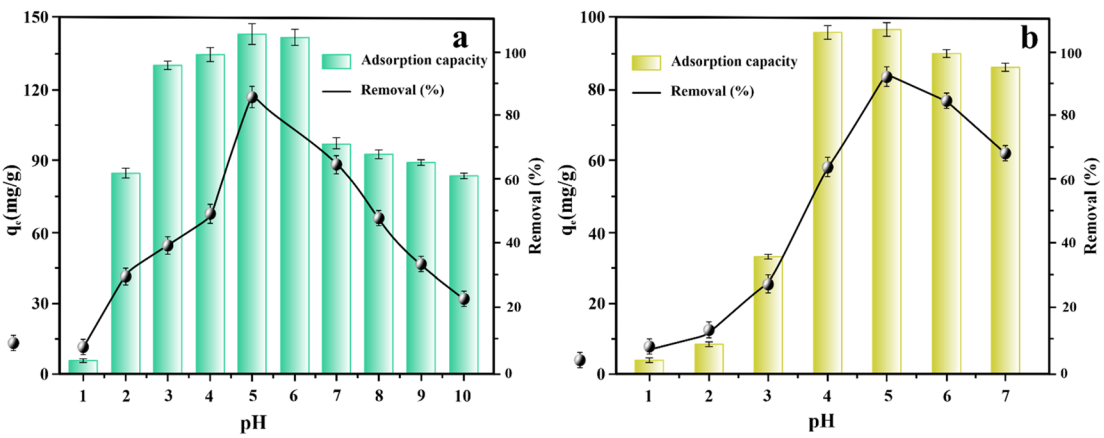

Fig. 5 Effect of pH on the adsorption of SMX (a) and Nd^{3+} (b) by the **FuS@MXene@AMP** composite.

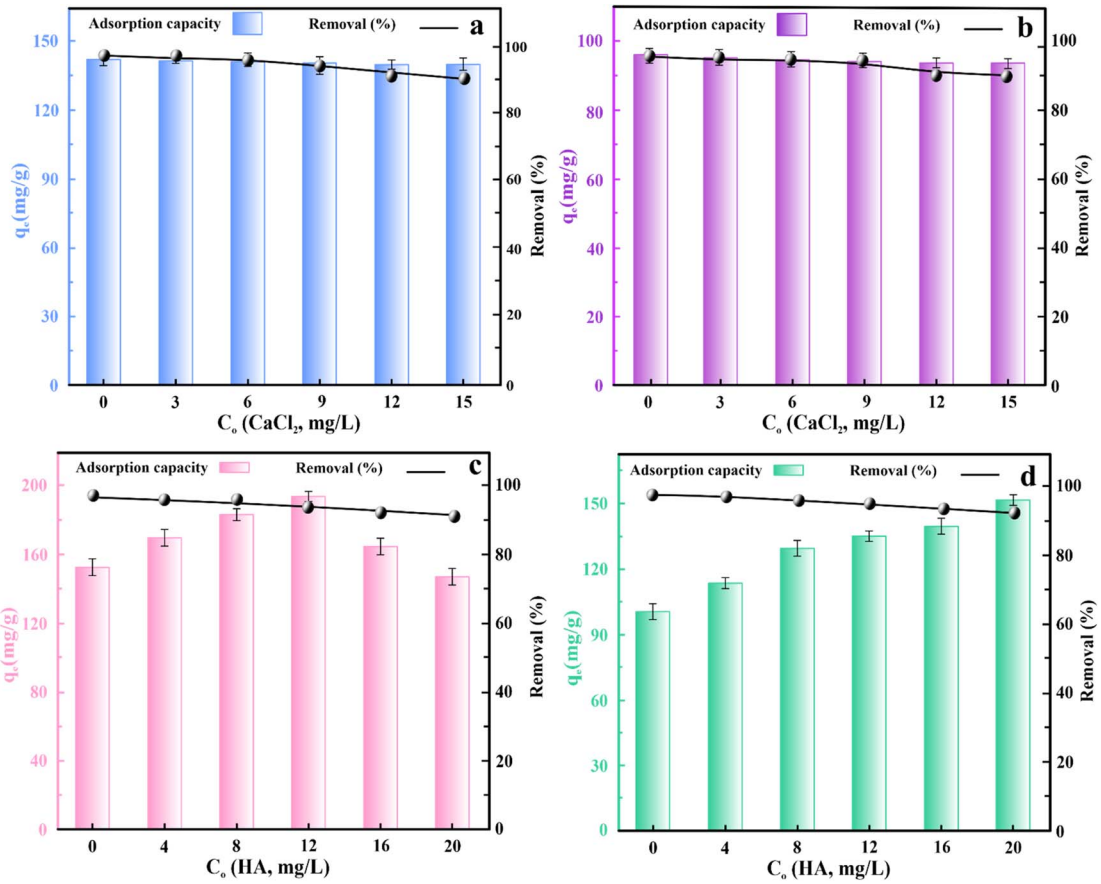

Fig. 6 Impact of $CaCl_2$ (a) on the adsorption of SMX (a) and Nd^{3+} (b) and impact of HA on the adsorption of SMX (c) and Nd^{3+} (d) by the FuS@MXene@AMP composite.

aminophosphonate. The potential bridging impact of humic acid between the adsorbent and SMX could account for the slightly enhanced adsorption performance at lower humic acid concentrations. HA competed for active adsorption sites with SMX at higher concentrations through principal interactions, such as electrostatic attraction and hydrogen bonding. Furthermore, the adsorption performance of Nd^{3+} ions by the adsorbent was observed with a rise in humic acid concentration from 0 to 20 mg L^{-1}, as depicted in Fig. 6(d). The carboxyl and phenolic groups of humic acid interact with Nd^{3+}; consequently, the adsorption capability of Nd^{3+} improved with increased humic acid concentration. The adsorption selectivity of the adsorbent for Nd^{3+} was also evaluated in a simulated acidic environment (acidity ~3 M HNO_3). The fixed adsorbent/liquid ratio used in adsorption experiments was 0.5 g L^{-1}. ICP-MS was utilized to determine the concentration of Nd^{3+} in the filtrate after removing the adsorbent using a 0.22 μm membrane filter.[71] The adsorption efficiency of the adsorbent for Nd^{3+} was above 99%, significantly higher than the other metal ions, indicating a distinct binding affinity of the adsorbent for Nd^{3+} (Fig. S4†). In this research work, we also compared the adsorption performance of **MXene**, **FuS**, **FuS@MXene**, and **FuS@MXene@AMP** for the elimination of SMX and Nd^{3+}. Owing to its greater surface area and higher adsorption sites (–Ti–O, C–F, $HOSO_3^-$, P═O, NH, and OH) than the **MXene** and **FuS**, **FuS@MXene** exhibited superior adsorption performance for SMX and Nd^{3+}, as depicted in Fig. S5(a and b).†

3.2.3. Kinetic study. In the adsorption kinetic study of **FuS@MXene@AMP**, three different initial SMX (40, 80, and 120 mg L^{-1}) or Nd^{3+} (25, 50, and 100 mg L^{-1}) concentrations were employed. The adsorption kinetic data was fitted using three well-known kinetic models, including the intraparticle diffusion model, pseudo-second-order, and pseudo-first-order rate models (Table S1†). For SMX, 90% of the adsorption process was completed in just 3 minutes, as exhibited in Fig. 7(a). The primary reason might be that the higher SMX concentration provided a potent mass transfer driving force during the initial sorption time, resulting in the fast occupation of SMX binding sites on **FuS@MXene@AMP**.[72,73] Moreover, **FuS@MXene@AMP** indicates an increased adsorption capacity of SMX as the concentration of SMX grows. For example, the **FuS@MXene@AMP** adsorbent's adsorption capacity for SMX was greater at 120 mg L^{-1} than at 40 and 80 mg L^{-1}. The primary reason could be that a greater concentration of SMX leads to a higher amount of SMX in the solution and a potent mass transfer driving force.[74] The results indicated that the PSO model was the most appropriate kinetic model for the adsorption of SMX among all the tested models.[75] It showed excellent

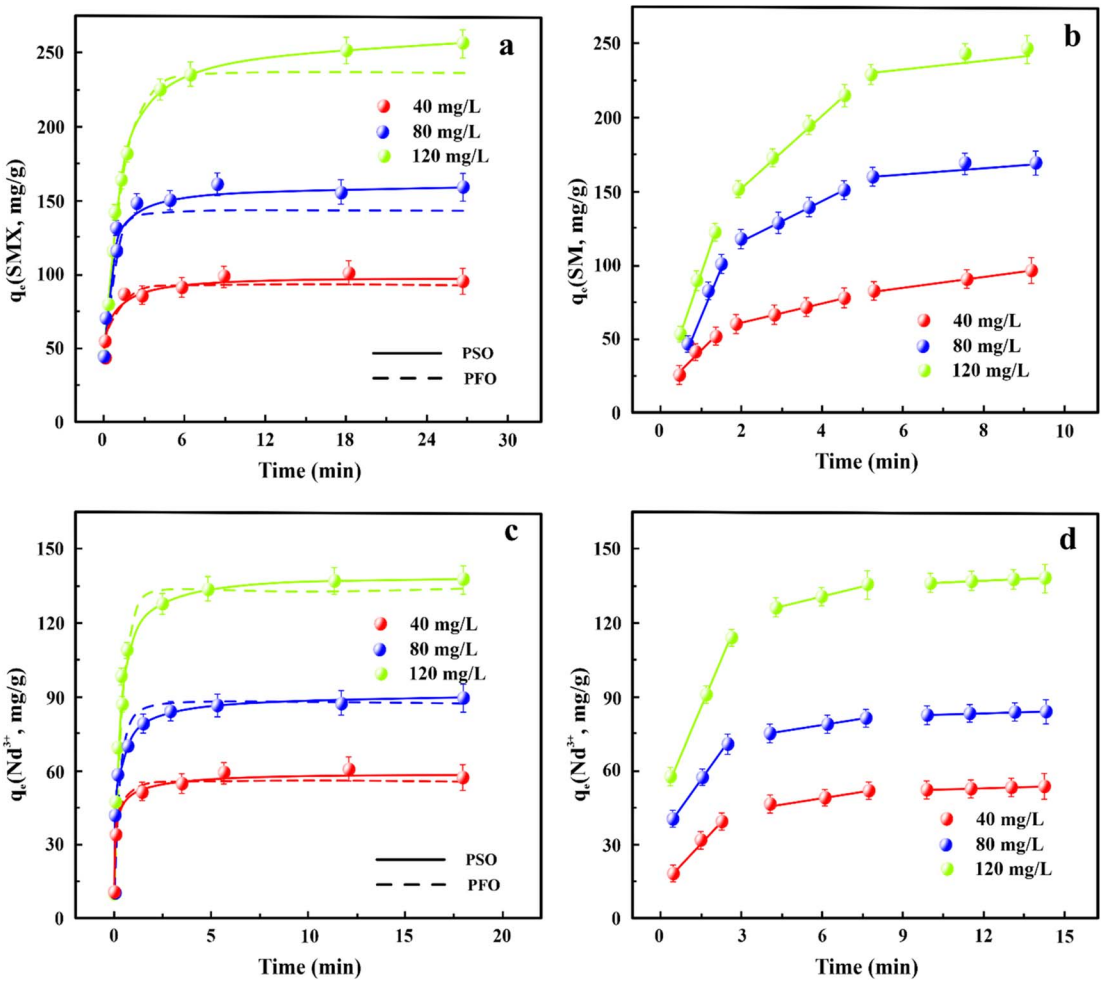

Fig. 7 Adsorption kinetics of the **FuS@MXene@AMP** adsorbent for SMX; PSO, PFO (a) and IPD (b) and Nd^{3+}; PSO and PFO (c) and IPD (d) onto the **FuS@MXene@AMP**.

agreement between the calculated and experimental data on the adsorption capacity, with the highest $R^2 = 0.9999$. We can, therefore, conclude that the adsorption of SMX is controlled by chemisorption. Nd^{3+} was adsorbed by the **FuS@MXene@AMP** adsorbent more quickly, as depicted in Fig. 7(c), and the adsorption reaction was nearly 90%, attained in just one minute. Furthermore, the PSO model accurately explained the adsorption of Nd^{3+}, suggesting that chemisorption played a dominant role in Nd^{3+} adsorption.[76] Table S2† lists the different kinetic parameters for various concentrations of SMX (40, 80, and 120 mg L^{-1}) and Nd^{3+} (25, 50, and 100 mg L^{-1}), where the maximum adsorption capacity achieved by PSO models was for SMX (99.94, 155.07, 252.32 mg g^{-1}) and Nd^{3+} (59.65, 90.05, 133.01 mg g^{-1}) respectively.

The IPD kinetic model for SMX and Nd^{3+} is illustrated in Fig. 7(b) and (d). Three stages comprise the adsorption process for SMX and Nd^{3+}: a fast stage at the beginning, an intermediate slower phase, and an equilibrium phase at the end. According to Table S3,† the values of the rate constant for the first phase ($k_{in}t_1$) were notably greater than the values of the second phase ($k_{in}t_2$) and third phase ($k_{in}t_3$), suggesting that the rate-controlling step for the adsorption of SMX and Nd^{3+} was primary film diffusion. Furthermore, in the adsorption of SMX and Nd^{3+}, no straight lines pass through the point of origin, indicating that the adsorption reaction was not only controlled by intraparticle diffusion but also involved some other diffusion processes, such as surface diffusion.[77]

3.2.4. Adsorption isotherm and thermodynamic study. Fig. 8(a and b) illustrates the isotherm investigation of the adsorbent for different initial contaminant concentration levels for a single system. Because contaminants are more mobile and more adsorption sites are available at higher dosages of pollutants, the adsorption capacity rises rapidly when the initial concentrations of contaminants grow.[78] To better comprehend the adsorption phenomena of SMX and Nd^{3+}, the adsorption experimental data were fitted and studied employing Freundlich and Langmuir's isotherm models (Table S4†). According to Fig. 8(a and b) and Table S5,† the correlation coefficient (R^2) values of the Freundlich model were higher compared to the Langmuir isotherm. This suggests that the adsorption of SMX by the **FuS@MXene@AMP** adsorbent was multilayer in nature. The higher affinity of the adsorbent toward SMX was described by the value of n (Freundlich isotherm model parameters). According to Table S5,† the value of n was higher than 1,

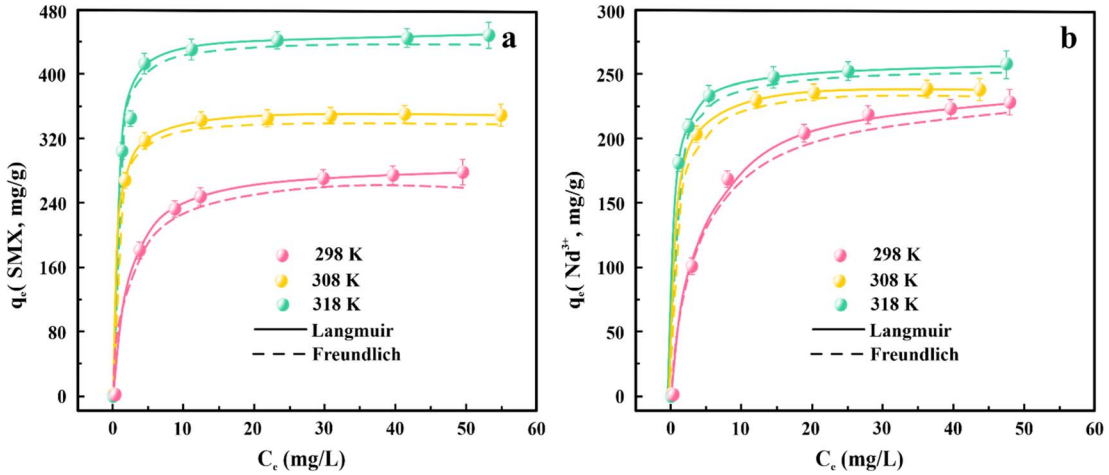

Fig. 8 Isotherm analysis of SMX (a) and Nd^{3+} (b) adsorption on the **FuS@MXene@AMP** composite.

implying that the adsorbent exhibited greater affinity for SMX. Furthermore, R_L determined from the Langmuir isotherm model fell within the range of 0 to 1, confirming that the adsorption of SMX and Nd^{3+} was proceeding positively.[79] The Langmuir model exhibited that SMX had a maximum adsorption capability of 448.91 mg g^{-1} at 318 K. Moreover, at low concentrations of 2 to 8 mg L^{-1}, the **FuS@MXene@AMP** ternary composite revealed remarkable adsorption efficiency for SMX, achieving an adsorption rate of 99%, indicating the significant potential of the **FuS@MXene@AMP** ternary composite for effective SMX adsorption (Fig. S6†). According to Fig. 8(a), SMX adsorption capability grew when the temperature increased from 298 K to 318 K, suggesting that the adsorption of SMX by the **FuS@MXene@AMP** adsorbent was heat-absorbing. According to Table S5,† the adsorption of Nd^{3+} is better explained by the Langmuir model with a higher value of adsorption capacity and R^2. This demonstrated that the uptake of Nd^{3+} by the adsorbent was mainly single-layer sorption. According to Fig. 8(b), Nd^{3+} adsorption capability increased when the temperature improved from 298 K to 318 K, implying that the adsorption of Nd^{3+} by the **FuS@MXene@AMP** adsorbent was endothermic in nature. Moreover, at 318 K, the maximum adsorption capability of Nd^{3+} was 255.78 mg g^{-1}, as per the Langmuir isotherm model. Compared to the previously reported adsorbents, **FuS@MXene@AMP** adsorbents demonstrated noticeably higher adsorption capacities for SMX and Nd^{3+}, as exhibited in Table S6.† For instance, Zhang *et al.* synthesized a rGO@([C·T·Nd]$_n$)re composite by self-assembly method for the adsorption of Nd^{3+}. The maximum adsorption capacity of rGO@([C·T·Nd]$_n$)re was 20.6 mg g^{-1}.[80] Javadian *et al.* developed a cross-linked composite incorporating polyamide, methine-thiophene, and pyrimidine (M-PPTA) for Nd^{3+} removal with a maximum adsorption capacity of 18.68 mg g^{-1}. With a 161.04 mg g^{-1} adsorption capacity, Burdzy *et al.* utilized iminodisuccinic acid (IDHA) for Nd^{3+} adsorption.[81] Chen *et al.* prepared an amino-grafted GO (GO-TYA) composite for the uptake of Nd^{3+} with an adsorption capacity of 80.66 mg g^{-1}.[82] The adsorption of **FuS@MXene@AMP** adsorbent for Nd^{3+} was 4.39, 13.69, 1.59, and 3.17 times of rGO@([C·T·Nd]$_n$)$_{re}$, M-PPTA, IDHA, and GO-TYA composite, respectively, which revealed the superior adsorption capacity of the **FuS@MXene@AMP** adsorbent compared to other adsorbents. The UiO-66-BC composites synthesized by Ouyang *et al.* exhibited 106.93 mg g^{-1} toward SMX.[83] The magnetic biochars (MBCs) were designed by Zhang *et al.* and proved to be effective for SMX adsorption with an adsorption capacity of 205 mg g^{-1}.[84] Jiao *et al.* prepared MIP@NH_2-UiO-66, which offered maximum adsorption of 68.36 mg g^{-1} for SMX. Ngo *et al.* prepared chitosan-modified biochar, which presented maximum adsorption of 14.73 mg g^{-1} for SMX. The adsorption of the **FuS@MXene@AMP** adsorbent for SMX was 4.20, 2.19, 6.57, and 30.47 times of UiO-66-BC, MBCs, MIP@NH_2-UiO-66, and chitosan-biochar composite, respectively, which revealed the superior adsorption capacity of the **FuS@MXene@AMP** adsorbent compared to other adsorbents.

To evaluate the thermodynamic properties of SMX and Nd^{3+}, various thermodynamic parameters, including enthalpy change (kJ mol^{-1}; ΔH°), Gibbs free energy (kJ mol^{-1}; ΔG°), and entropy change (ΔS°; J mol K^{-1}), were calculated employing the following equation.

$$\Delta G^\circ = -RT \ln K_D \quad (1)$$

$$K_D = \frac{q_e}{C_e} \quad (2)$$

$$\Delta G^\circ = \Delta H^\circ + T\Delta S \quad (3)$$

T (K) is the absolute temperature and R (J mol^{-1} K^{-1}) is the ideal gas constant. The values of ΔS° and ΔH° were determined by utilizing the slope and intercept of the $\ln K_{D-1}/T$ plot, respectively.

The thermodynamic investigation is essential to comprehending the sorption mechanism. Table S7† shows that the changes in Gibbs free energy ($\Delta G < 0$) were negative at different temperatures, suggesting that **FuS@MXene@AMP** spontaneously adsorbed SMX and Nd^{3+}. The adsorption of SMX and Nd^{3+}

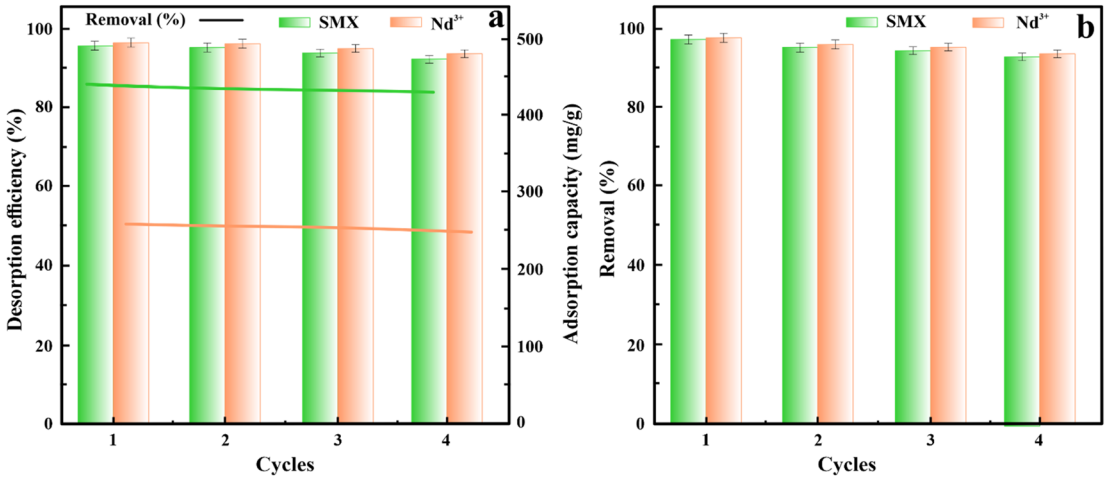

Fig. 9 The influences of regeneration on FuS@MXene@AMP adsorption capacity and desorption performance (a) and its use in simulated real wastewater (b).

was irreversible, as demonstrated by the positive change in entropy. The adsorption process was endothermic, as indicated by the positive values of the enthalpy change.

3.2.5. Desorption, regeneration, and reusability of FuS@MXene@AMP and its practical application in model wastewater. A mixed solution of ethanol and HCl in a volume ratio of 1 : 1 is employed to accomplish SMX desorption.[85] A 0.2 M HCl solution is employed to attain Nd^{3+} desorption.[86] After adsorption of Nd^{3+} and SMX in a mono-pollutant or binary pollutant system, the spent **FuS@MXene@AMP** adsorbent was recovered using centrifugation, rinsed with excessive Milli-Q water, and thereafter submerged in HCl (in the case of Nd^{3+}) or in a mixed solution of ethanol and HCl (in the case of SMX) and agitated for two hours at ambient temperature, performed three times, cleaned again with DI water, and finally vacuum-dried at 60 °C overnight. The recovered adsorbent was utilized to adsorb naproxen under identical experimental circumstances. The adsorption and desorption analyses are performed in four consecutive cycles. Eqn (4) and (5) are employed to calculate the desorption efficiency and regeneration rate (%).

$$\mathrm{DE}(\%) = \frac{C_\mathrm{D} \times V \times 100}{q_\mathrm{d} \times m_\mathrm{d}} \quad (4)$$

$$\mathrm{RE}(\%) = \frac{q_\mathrm{d} \times 100}{q_\mathrm{e}} \quad (5)$$

Here, q_d indicates the adsorption capacities of the SMX-loaded **FuS@MXene@AMP** and Nd^{3+}-loaded **FuS@MXene@AMP** before the desorption study in mg g^{-1}, q_e defines the sorption capacity at the first test in mg g^{-1}, C_D represents the metal ion and antibiotics concentration (m L^{-1}), V denotes the volume in L, and shows the **FuS@MXene@AMP** amount employed in the desorption investigations. The ability of an adsorbent to regenerate and absorb pollutants from actual wastewater is an essential factor to consider when evaluating it for practical use. As depicted in Fig. 9(a), slight declines in the sorption capacities of the **FuS@MXene@AMP** for SMX and Nd^{3+} were recorded after four adsorption–desorption analyses in the wastewater. Fig. 9(a) depicts that the as-synthesized **FuS@MXene@AMP** composite demonstrates the ability to maintain >92% of its initial sorption capability and desorption performance for SMX and Nd^{3+}.

The ability of **FuS@MXene@AMP** to remove SMX and Nd^{3+} and its regeneration capability is investigated in simulated water. The detailed process for the preparation of simulated water is provided in Text S4.†Fig. 9(b) illustrates that at a concentration of 5 g L^{-1} of the **FuS@MXene@AMP** composite, the adsorption rates for SMX and Nd^{3+} are up to 92%. Following regeneration, the adsorption rate of the composites for SMX and Nd^{3+} slightly decreased. As a result, **FuS@MXene@AMP** also demonstrated remarkable regeneration ability and adsorption performance in the simulated model wastewater.

3.2.6. Analysis of the adsorption performance of the adsorbent in binary systems of SMX and Nd^{3+}. The investigation of the capacity of the composites to remove combined pollutants simultaneously is illustrated in Fig. 10(a and b). This study was carried out for binary systems that consisted of SMX–Nd^{3+} and Nd^{3+}–SMX. This study examined the mutual interactions and effects of pollutants in antibiotic-heavy metal binary systems. Therefore, to understand more about the sorption of SMX and Nd^{3+}, the sorption capability ratio (R_q) was calculated using the equation below.

$$R_\mathrm{q} = \frac{q_{\mathrm{b},i}}{q_{\mathrm{m},i}} \quad (6)$$

$q_{\mathrm{b},i}$ denotes the SMX and Nd^{3+} sorption capability in the antibiotic-heavy metal binary systems in mg g^{-1}. $q_{\mathrm{m},i}$ represents the mono-pollutant system in mg g^{-1}.

Depending on the value of R_q, the simultaneous adsorption of multiple pollutants can be divided into three categories. Synergism (where $R_\mathrm{q} > 1$) enhances the adsorbent's ability to adsorb the target adsorbate, antagonism (where $R_\mathrm{q} < 1$), where the adsorbent's ability to adsorb the target adsorbate is reduced when a co-adsorbate is present, and non-interacting (where $R_\mathrm{q} = 1$). Fig. S7(a and b)† displays the determined R_q values based

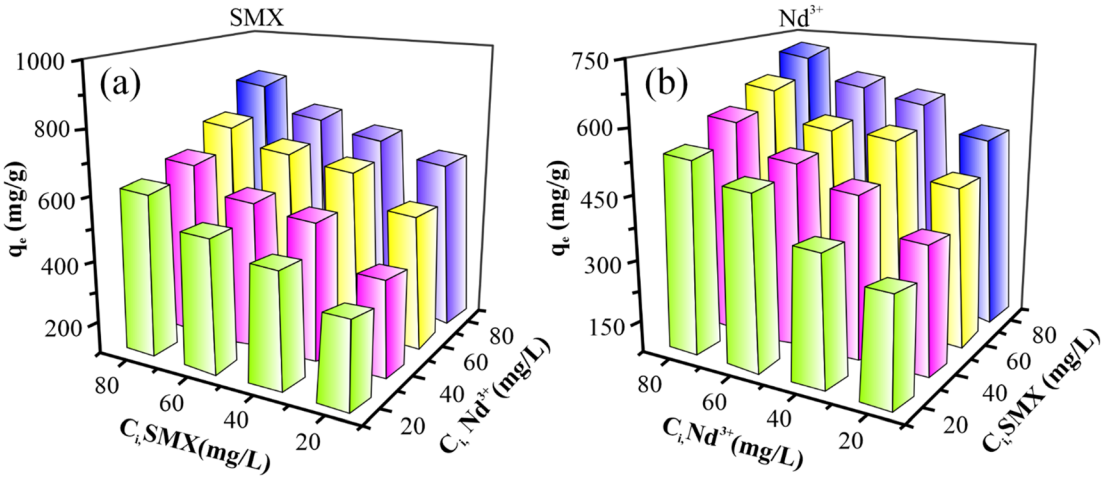

Fig. 10 Simultaneous adsorption of SMX (a) and Nd^{3+} (b) onto the **FuS@MXene@AMP** composite in SMX–Nd^{3+}(a) and Nd^{3+}–SMX binary solutions.

on the initial SMX and Nd^{3+} concentrations. The co-occurrence of Nd^{3+} remarkably increased the adsorption of SMX in the SMX–Nd^{3+} pollutant systems (R_q, SMX > 1). In the antibiotic-heavy metal binary pollutant solution systems, the occurrence of Nd^{3+} notably enhanced the adsorption capacity of SMX, especially at higher concentrations of Nd^{3+}. This phenomenon may be caused by several reactions during the adsorption of SMX in the presence of Nd^{3+}. Firstly, the medium influence of Nd^{3+} in the SMX adsorption phenomenon enhanced the adsorption capability of SMX. Nd^{3+} exhibited coordination with SMX and formed bonds with OH, NH, $HOSO_3^-$, F, O, and S on the adsorbent surface, utilizing the multifunctional characteristics of the antibiotics. Multiple reports have demonstrated that these functional groups cause drugs to bind to other materials, mainly metal ions, to form antibiotic-metal ion complexes.[87–90] SMX might also interact with metal hydroxide by coordination, indirectly bound to the composite, and synergistically eliminated, in addition to the phenomena entailed in the direct actions of **FuS@MXene@AMP** in mono-pollutant systems.[61] Another effective mechanism might include the generation of an antibiotic-metal combination between SMX and Nd^{3+} before being adsorbed on the **FuS@MXene@AMP** adsorbent surface.[91] Notably, at a lower concentration of Nd^{3+}, the R_q value for SMX was less than 1. Thus, we can say that the "medium" role of metal ions (Nd^{3+}) was not possible at lower Nd^{3+} concentrations. For this scenario, a minute dose of Nd^{3+} was first attached to SMX in the solution, generating an Nd^{3+} + SMX combination, then attached to the **FuS@MXene@AMP** composite surface to be removed.

Like SMX, the adsorbent's Nd^{3+} adsorption capability in the Nd^{3+}–SMX binary system was also higher than that of the mono-pollutant system (R_q, Nd^{3+} > 1), as exhibited in Fig. S7(a and b).† The adsorption of other metal ions, such as Ca^{2+} and Al^{3+}, in the presence of SMX was investigated. The presence of SMX synergistically enhanced the adsorption of Ca^{2+} and Al^{3+}, as shown by the R_q values exceeding 1 (Fig. S8†). The presence of multiple functional groups in SMX antibiotics adsorbed on the **FuS@MXene@AMP** composite surface, where additional oxygenous and nitrogenous functional groups were available, potentially describes this synergistic interaction and facilitates the adsorption of Nd^{3+}, Ca^{2+}, and Al^{3+}.

3.2.7. Method validation. To assess the analytical performance of the method, the limits of detection (LOD) and limits of quantification (LOQ), linear range, recovery, and correlation coefficient (R^2) were studied. The obtained results are listed in Table S8.† The linear ranges were 1–50 μg L^{-1} and 2.0–100 μg L^{-1} for SMX and Nd^{3+}, with R^2 values of 0.9920 and 0.9982, respectively. The LOD and LOQ values for SMX were 5 and 25 μg L^{-1}, while for Nd^{3+}, they were 0.80 and 5.2 μg L^{-1}. The outcomes demonstrated that the pollutant recoveries ranged from 87.6% to 93.2%.

3.2.8. Adsorption of mechanisms

3.2.8.1. Possible adsorption mechanism for neodymium (Nd^{3+}). Two types of interactions, such as metal complexation and electrostatic interactions, are involved in the adsorption of Nd^{3+}, as exhibited in Fig. 13. XPS and FTIR analyses were conducted before or after the adsorption to describe the possible adsorption mechanism of Nd^{3+} by the **FuS@MXene@AMP** adsorbent. The FTIR peaks for Ti–O, C–F, $HOSO_3^-$, P=O, NH, and OH groups shifted from 623, 1119, 1237, 1275, 1614, and 3428 cm^{-1} to 614, 1108, 1223, 1255, 1602, and 3410 cm^{-1}, respectively (Fig. S9†). The shifting of the FTIR peaks of these functional groups of the **FuS@MXene@AMP** adsorbent suggested the electrostatic attraction between Nd^{3+} and Ti–O, C–F, $HOSO_3^-$, P=O, NH, and OH. Consequently, the electrostatic attraction was a dominant force for the adsorption of Nd^{3+} due to the sufficient electronegativity difference between the Ti–O, C–F, $HOSO_3^-$, P=O, NH, and OH groups of adsorbents and Nd^{3+} metal ions. For instance, the electronegativity differences are 1.35, 3.84, 1.44, 1.25, 1.90, and 2.30 between Ti–O, C–F, $HOSO_3^-$, P=O, NH, and OH groups of **FuS@MXene@AMP** and Nd^{3+}, respectively. XPS analysis was further used to investigate the adsorption mechanism of Nd^{3+} before or after adsorption. Three prominent peaks are visible in the C 1s spectra of the

FuS@MXene@AMP composite at binding energies of 284.28 (C–H and C–C), 285.69 (C–OH, C–S, and C–P), and 287.20 eV (C═O, C–O–P, and C–O–C), as exhibited in Fig. 2(a). After the adsorption of Nd^{3+}, the binding energies shift from 284.28, 285.69, and 287.20 eV to 284.01, 285.18, and 287.00 eV, respectively (Fig. 11(a)). The findings show that the CH, C–C, C–OH, C–S, C–P, C═O, C–O–P, and C–O–C functional groups present in **FuS@MXene@AMP** adsorbed Nd^{3+} pollutants *via* electrostatic interaction and metal complexation. The high-resolution XPS spectra of the **FuS@MXene@AMP** composites showed three characteristic XPS peaks in the O 1s region, which correspond to the P–O–C or P═O, C═O, and OH groups (Fig. 2(b)). Originally, these XPS peaks were detected at the binding energies of 530.51, 532.31, and 532.94 eV, respectively.[92] After Nd^{3+} adsorption, the three peaks were shifted to 530.31, 532.04, and 532.76 eV (Fig. 11(b)). These shifts in binding energies of P═O, C═O, OH, and P–O–C groups of the **FuS@MXene@AMP** composites confirmed the vital role of oxygen-containing groups in the adsorption of Nd^{3+}. Two distinct peaks assigned to the NH_2 or NH and NH^{2+} or NH^{3+} groups are visible in the XPS survey spectra of **FuS@MXene@AMP** composites in the N 1s region, as illustrated in Fig. 2(c). Before the adsorption of Nd^{3+}, the binding energies were identified at 399.57 and 401.92 eV, respectively. After the adsorption of Nd^{3+}, these XPS peaks were shifted to 399.43 and 401.76 eV for Nd^{3+} (Fig. 11(c)). The XPS survey spectra of the **FuS@MXene@AMP** composite in the S 2p region showed three characteristic peaks attributed to the C–S, C═S, and S–O ($2p_{3/2}$) groups, as shown in Fig. 2(d). Before the adsorption of Nd^{3+}, these peaks were identified at binding energies of 161.23, 163.54, and 166.81 eV, respectively. After successful sorption of Nd^{3+}, the three XPS peaks shifted to 161.01, 163.28, and 166.63 eV Fig. 11(d). The results suggested that the nitrogen- and sulfur-containing functional groups of the composites play a role in the adsorption of Nd^{3+}.

3.2.8.2. Possible adsorption mechanism for SMX. The PSO model was well fitted with the experimental uptake data of SMX, indicating that SMX was chemically adsorbed on the adsorbent surface, which may include hydrogen bonding and π–π interactions. The change in the peak positions of functional groups of the adsorbent was assessed after the adsorption of SMX through the FTIR study. The peaks in the FTIR spectrum of **FuS@MXene@AMP**-SMX were shifted from 623, 1119, 1237, 1275, 1614, and 3428 cm^{-1} to 619, 1113, 1229, 1267, 1609, and 3419 cm^{-1}, corresponding to the Ti–O, C–F, $HOSO_3^-$, P═O, NH, and OH groups, respectively (Fig. S9†). The SMX molecules consist of SO_2NH_2, NH_2, CH_3, and C_3H_3NO groups, as shown in Fig. 13. The adsorption process of SMX was facilitated by the Ti–O, C–F, $HOSO_3^-$, P═O, NH, and OH groups of the adsorbent forming hydrogen bonds with SO_2NH_2, NH_2, CH_3, and C_3H_3NO of SMX. After the adsorption of SMX, peaks were shifted from 1580 to 1568 cm^{-1}, attributing to the C═C aromatic functional group, which indicated the π–π interaction between the

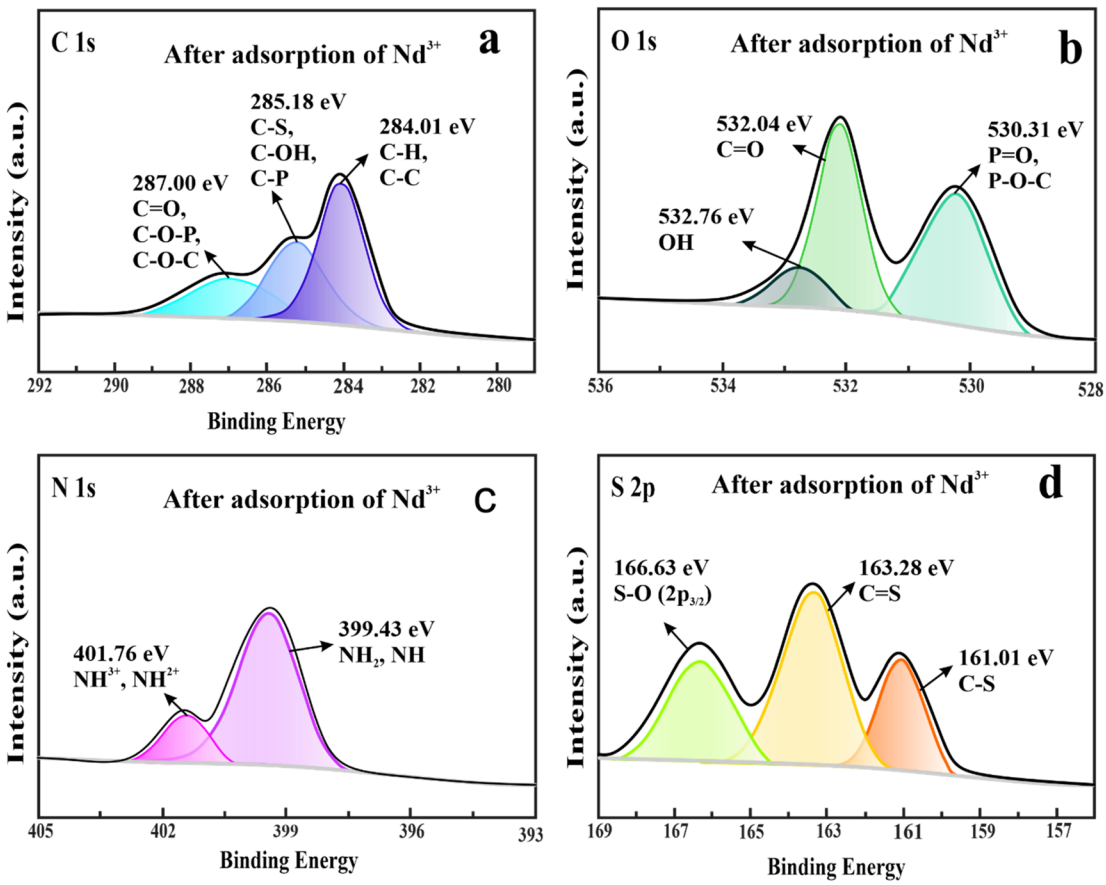

Fig. 11 High-resolution XPS survey spectra of C 1s (a), O 1s (b), N 1s (c), and S 2p (d) after adsorption of Nd^{3+}.

prepared adsorbent consisting of the aromatic ring and benzene ring of SMX.[93] XPS spectra results help further explore the SMX adsorption mechanisms. After SMX uptake, the binding energies of CH, C–C, C–OH, C–S, C–P, C=O, C–O–P, C–O–C, C–OH, C–S, and C–P were shifted from 284.28, 285.69, and 287.20 eV to 284.01, 285.36, and 287.05 eV, respectively (Fig. 12(a)). The adsorption of SMX was promoted by the CH, C–C, C–OH, C–S, C–P, C=O, C–O–P, and C–O–C functional groups of the adsorbent through hydrogen bonding and π–π interactions. The peaks of P–O–C, or P=O, C=O, and OH groups originally appeared at 530.51, 532.31, and 532.94 eV before adsorption in the O 1s spectra and were shifted to 530.45, 532.22, and 532.89 eV after adsorption of SMX, respectively (Fig. 12(b)), suggesting that P–O–C, or P=O, C=O, and OH of the adsorbent form hydrogen bonding with SO_2NH_2, NH_2, CH_3, and C_3H_3NO of SMX. In the N 1s region, two distinct peaks corresponding to the NH_2 or NH and NH^{2+} or NH^{3+} groups were observed at 399.57 and 401.92 eV. After the adsorption of SMX, these XPS peaks were shifted to 399.49 and 401.85 eV Fig. 12(c). The peaks of C–S, C=S, and S–O ($2p_{3/2}$) groups were identified at binding energies of 161.23, 163.54, and 166.81 eV in the s 2p spectra before adsorption, and these peaks shifted to 161.09, 163.48, and 166.74 eV after the adsorption of SMX, respectively (Fig. 12(d)). The results indicated that the nitrogen- and sulfur-containing functional groups of **FuS@MXene@AMP** were involved in the adsorption of SMX through hydrogen bonding.

3.2.8.3. Possible adsorption mechanism for the binary pollutant system. The co-occurrence of Nd^{3+} remarkably increased the adsorption of SMX in the SMX–Nd^{3+} pollutant systems. The occurrence of Nd^{3+} and SMX in the solution notably enhanced the adsorption capacity of SMX or Nd^{3+}. This might be due to the following types of interactions:

(a) The medium effect of Nd^{3+} in the adsorption process increased the adsorption capacity for SMX. Specifically, in addition to interacting with Ti–O, C–F, $HOSO_3^-$, P=O, NH, and OH groups on the adsorbent, parts of Nd^{3+} could bind with SMX.[94]

(b) Firstly, SMX was adsorbed on the adsorbent surface through hydrogen bonding or π–π interaction, then SMX bound with Nd^{3+} through electrostatic interactions rather than directly interacting with the adsorbent like single pollutant systems.[78]

(c) Another effective mechanism might include the formation of an antibiotic-metal combination between SMX and Nd^{3+} before being adsorbed on the **FuS@MXene@AMP** adsorbent surface.[91]

FTIR and XPS analyses were used to explore the adsorption mechanism for the binary system. Fig. S9† shows the spectral changes that occur for binary pollutant systems following the adsorption of SMX + Nd^{3+}. FTIR peaks for Ti–O, C–F, $HOSO_3^-$, P=O, NH, and OH groups shifted to lower wave numbers after the SMX + Nd^{3+} were absorbed, suggesting that these functional

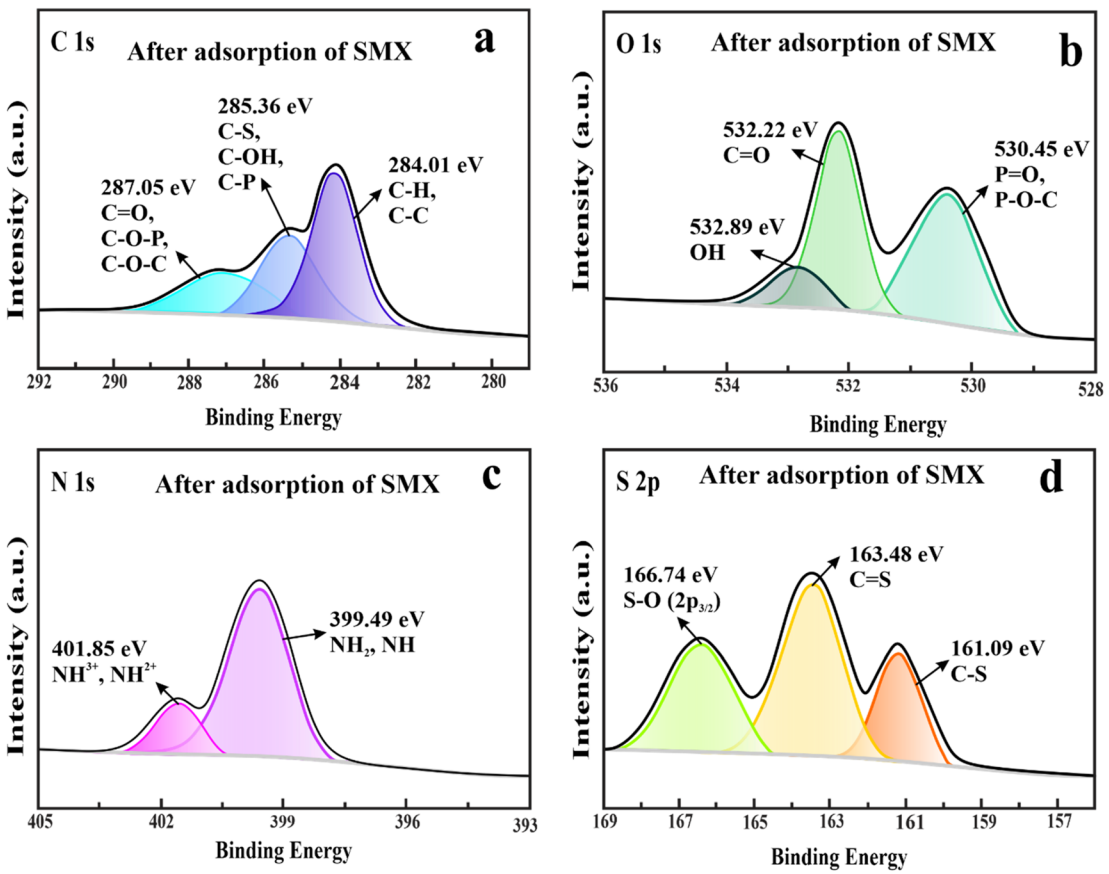

Fig. 12 High-resolution XPS survey spectra of C 1s (a), O 1s (b), N 1s (c), and S 2p (d) after adsorption of SMX.

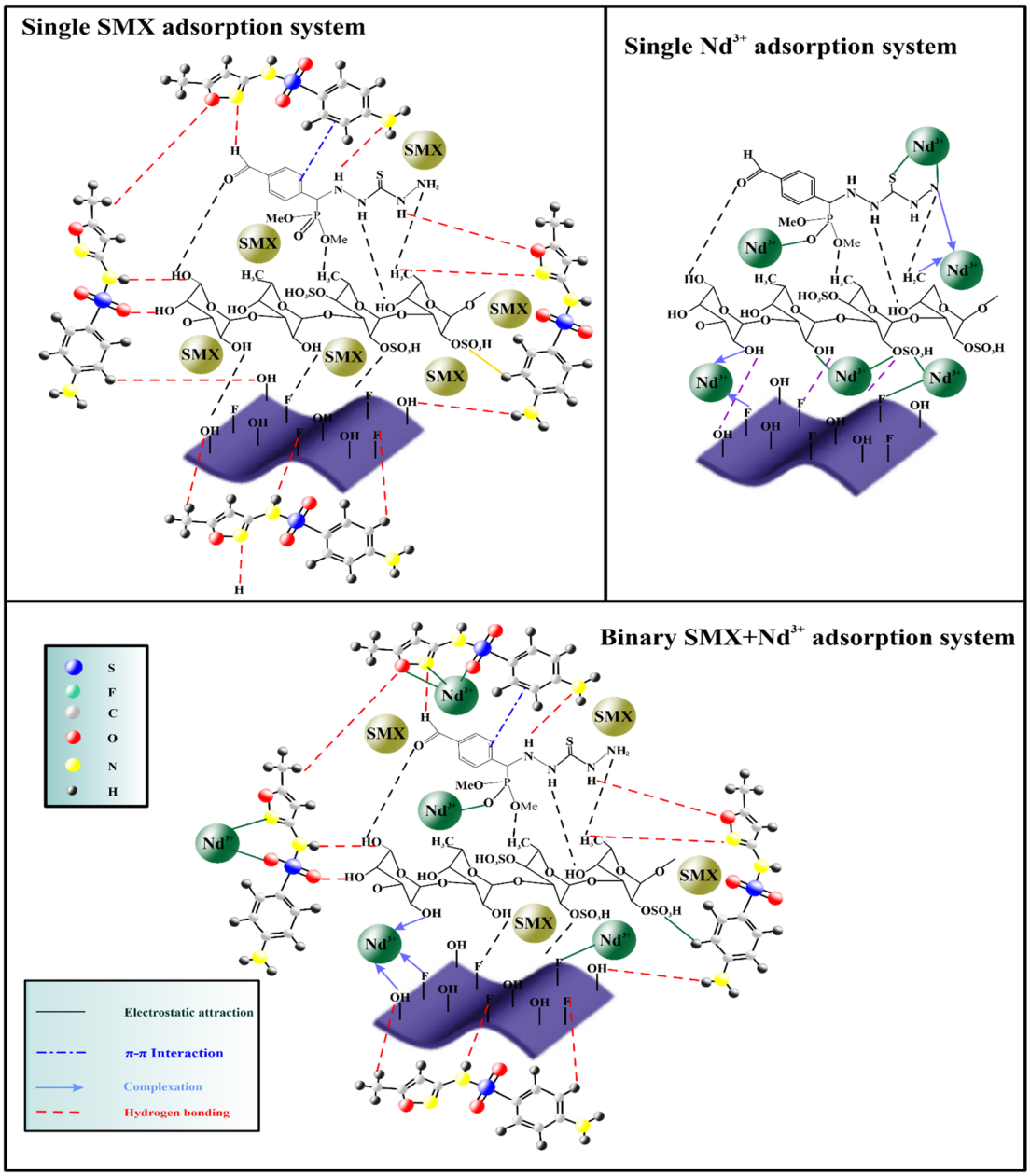

Fig. 13 Possible mechanism of adsorption of SMX and Nd^{+} in mono- and binary contaminant systems using the FuS@MXene@AMP composite.

groups are involved in the adsorption of SMX + Nd^{3+} pollutants. After the simultaneous uptake of SMX and Nd^{3+} from the binary pollutant system, the binding energies of CH, C–C, C–OH, C–S, C–P, C=O, C–O–P, C–O–C, C–OH, C–S, and C–P were moved from 284.28, 285.69, and 287.20 eV to 283.99, 285.02, and 286.96 eV, respectively (Fig. S10(a)†). The peaks of P–O–C, or P=O, C=O, and OH groups initially emerged at 530.51, 532.31, and 532.94 eV before adsorption in the O 1s spectra and were shifted to 530.68, 531.99, and 532.68 eV after the adsorption of SMX + Nd^{3+}, respectively (Fig. S10(b)†). In the N 1s region, two distinct peaks corresponding to the NH_2 or NH and NH_2^{+} or NH_3^{+} groups were seen at 399.59 and 401.92 eV. After capturing SMX + Nd^{3+}, these XPS peaks were shifted to 399.28 and 401.59 eV (Fig. S10(c)†). The peaks of C–S, C=S, and S–O ($2p_{3/2}$) groups were detected at 161.23, 163.54, and 166.81 eV in the S 2p spectra before adsorption, and these peaks shifted to 160.99, 163.10, and 166.01 eV after the adsorption of SMX + Nd^{3+}, respectively (Fig. S10(d)†). The shifting of peaks in the C 1s, O 1s, N 1s, and S 2p high-resolution spectra suggested that the carbon-, oxygen-, nitrogen-, and sulfur-containing functional groups of composites play a part in the adsorption of SM + Nd^{3+} (Fig. 13).

4 Conclusion

The efficient adsorption of SMX and Nd^{3+} from wastewater was conducted by preparing an unexplored **FuS@MXene@AMP** adsorbent. Over a wide pH range, the **FuS@MXene@AMP**

adsorbent exhibited an excellent ability to remove SMX and Nd^{3+} in mono and binary pollutant systems. A pseudo-first-order (PSO) kinetic model was the most appropriate for describing the adsorption of SMX and Nd^{3+} among all the tested kinetic models. With a higher value of adsorption capacity and R^2, the Langmuir isotherm model provided a better description of the adsorption of SMX and Nd^{3+}. Compared to the previously reported adsorbents, **FuS@MXene@AMP** adsorbents demonstrated noticeably higher adsorption capacities for SMX and Nd^{3+}. Furthermore, it was found that **FuS@MXene@AMP** exhibited higher adsorption performance even after undergoing 4 cycles in wastewater simulation. This result demonstrates its applicability and reusability in wastewater treatment procedures. In binary SMX + Nd^{3+} pollutant systems, **FuS@MXene@AMP** indicates excellent ability for simultaneous adsorption of coexisting Nd^{3+} and SMX from wastewater. The improved adsorption performance was primarily due to the synergistic interaction of SMX and Nd^{3+}. The results of FTIR and XPS studies indicated that the removal mechanisms were primarily based on hydrogen bonding, π–π interaction, complexation, and electrostatic interactions. This research provides a practical strategy for designing new adsorbents that can efficiently adsorb heavy metals and antibiotics over a broad pH range.

Data availability

The data supporting this article have been included as part of the ESI.†

Author contributions

Aysha Bukhari: data curation, supervision, writing original draft, reviewing, and editing, Irfan Ijaz: formal analysis, visualization, writing original draft, reviewing, and editing, Ezaz Gilani: reviewing, and editing, and methodology, Ammara Nazir: writing original draft, software, and investigation, Hina Zain: data curation and investigation, Attia Shaheen: formal analysis, and methodology, Mohammed Rafi Shaik: investigation and validation, Mujeeb Khan: reviewing, and editing and data curation, Jilani P. Shaik: formal analysis and resource.

Conflicts of interest

The authors declare that they have no known competing financial interests or personal relationships that could have appeared to influence the work reported in this paper.

Acknowledgements

The authors acknowledge the funding from Researchers Supporting Project number (RSPD2025R665), King Saud University, Riyadh, Saudi Arabia. All authors also acknowledge the School of Chemistry, Minhaj University Lahore, Pakistan, for providing a platform for this work.

References

1 Q. Fan, C. Sun, B. Hu and Q. Wang, *Mater. Today Bio*, 2023, **20**, 100646.
2 S. Sun, M. Chen, X. Dao, L. Wang, X. Huang, L. Zhou and H. Hao, *Sep. Purif. Technol.*, 2023, **306**, 122537.
3 D. Liu, X. Wu, C. Hu, Y. Zeng and Q. Pang, *Aquat. Toxicol.*, 2023, **261**, 106621.
4 Y. Yang, A. Walton, R. Sheridan, K. Güth, R. Gauß, O. Gutfleisch, M. Buchert, B.-M. Steenari, T. Van Gerven and P. T. Jones, *J. Sustain. Metall.*, 2017, **3**, 122–149.
5 N. Radwan-Pragłowska, J. Radwan-Pragłowska, K. Łysiak, Ł. Janus and T. Galek, *Opt. Laser Technol.*, 2024, **174**, 110611.
6 T. Cheisson and E. J. Schelter, *Science*, 2019, **363**, 489–493.
7 T. Yao, Y. Geng, J. Sarkis, S. Xiao and Z. Gao, *Resour., Conserv. Recycl.*, 2021, **174**, 105752.
8 S.-L. Liu, H.-R. Fan, X. Liu, J. Meng, A. R. Butcher, L. Yann, K.-F. Yang and X.-C. Li, *Ore Geol. Rev.*, 2023, **157**, 105428.
9 Y. Chen and B. Zheng, *Sustainability*, 2019, **11**, 1288.
10 B. Qin, B. Wang, J. Li, T. Wang and X. Xu, *Sep. Purif. Technol.*, 2024, **342**, 126905.
11 X. Chen, F. Duan, X. Yu, Y. Xie, Z. Wang, A. El-Baz, B.-J. Ni and S.-Q. Ni, *Water Res.*, 2024, **265**, 122268.
12 I. Ijaz, A. Bukhari, A. Shaheen, A. Nazir, E. Gilani, H. Zain, S. Muhammad and S. Hussain, *J. Environ. Chem. Eng.*, 2024, 112838.
13 K. Burdzy, R. Jastrząb and D. Kołodyńska, *Chem. Eng. J.*, 2024, **479**, 147632.
14 R. Antonelli, G. R. P. Malpass and A. C. S. C. Teixeira, *Sep. Purif. Technol.*, 2024, **330**, 125290.
15 K. Lu, J. Qin, M. Hu, L. Hu, M. Mao, X. Li, Z. Lin and W. Liu, *Environ. Sci.:Nano*, 2024, **11**, 900–910.
16 Z. Qu, R. Leng, S. Wang, Z. Ji and X. Wang, *Rev. Environ. Contam. Toxicol.*, 2024, **262**, 1–37.
17 M. Nogueira, I. Matos, M. Bernardo, L. A. C. Tarelho, A. M. Ferraria, A. M. B. do Rego, I. Fonseca and N. Lapa, *J. Waste Manage.*, 2024, **174**, 451–461.
18 S. Kathi and A. E. D. Mahmoud, *Desalin. Water Treat.*, 2024, 100258.
19 I. Ijaz, A. Bukhari, A. Nazir, E. Gilani, H. Zain, S. Hussain and H. Ahmad, *Mater. Chem. Phys.*, 2024, **314**, 128929.
20 J. Yu, Y. Xia, L. Chen, W. Yan, B. Liu and S. Jin, *npj Clean Water*, 2024, **7**, 133.
21 I. Liaquat, R. Munir, N. A. Abbasi, B. Sadia, A. Muneer, F. Younas, M. F. Sardar, M. Zahid and S. Noreen, *Environ. Pollut.*, 2024, 123922.
22 U. Tyagi and N. Anand, *Waste Manag. Bull*, 2024, **2**, 308–325.
23 Y. Wang, J. Wu, W. Zhang, L. Zhong, D. Zhang, S. Yan and J. Shi, *React. Chem. Eng.*, 2024, **9**, 1276–1291.
24 Y. S. Giri, A. Subash and B. Kandasubramanian, *Hybrid Adv.*, 2024, 100237.
25 N. A. Efiana, G. Kali, A. Fürst, A. Dizdarević and A. Bernkop-Schnürch, *Eur. J. Pharm. Sci.*, 2023, **180**, 106313.
26 N. Jabeen and M. Atif, *Polym. Adv. Technol.*, 2024, **35**, e6203.
27 Q. Liu, L. Hu, C. Wang, M. Cheng, M. Liu, L. Wang, P. Pan and J. Chen, *Int. J. Biol. Macromol.*, 2023, **225**, 526–543.

28 L. Sun, Z. Jiang, B. Yuan, S. Zhi, Y. Zhang, J. Li and A. Wu, *Chem. Eng. Res. Des.*, 2021, **174**, 71–78.
29 G. Chen, L. Yu, F. Shi, J. Shen, Y. Zhang, G. Liu, X. Mei, X. Li, X. Xu and C. Xue, *Carbohydr. Polym.*, 2024, 122345.
30 S. B. Kim, M. Farrag, S. K. Mishra, S. K. Misra, J. S. Sharp, R. J. Doerksen and V. H. Pomin, *Carbohydr. Polym.*, 2023, **301**, 120316.
31 Q. Hu, L. Li, J. Li, X. Sun, C. Yan, M. Mao, Z. Lin and W. Liu, *ACS ES&T Eng.*, 2024, **4**, 1657–1667.
32 D. P. Nagahawatta, N. M. Liyanage, T. U. Jayawardena, F. Yang, H. Jayawardena, M. Kurera, F. Wang, X. Fu, Y.-J. Jeon and D. P. Nagahawatta, *Algae*, 2023, **38**, 217–240.
33 Z.-B. Wang, J. Zhang, Q. Miao, H.-Y. Cao, F. Xiong, T. Lee, A. El-Baz, L. Xie and S.-Q. Ni, *Environ. Sci. Technol.*, 2024, **58**, 21242–21250.
34 S. Li, J. Li, Z. Zhi, C. Wei, W. Wang, T. Ding, X. Ye, Y. Hu, R. J. Linhardt and S. Chen, *Carbohydr. Polym.*, 2017, **173**, 330–337.
35 U. Adhikari, C. G. Mateu, K. Chattopadhyay, C. A. Pujol, E. B. Damonte and B. Ray, *Phytochemistry*, 2006, **67**, 2474–2482.
36 Y. Cai, W. Yang, R. Yin, L. Zhou, Z. Li, M. Wu and J. Zhao, *Carbohydr. Res.*, 2018, **464**, 12–18.
37 J. Deng, H. Wang, R. Gao, X. Ma, M. Chen, D. Xu and A. Cai, *J. Environ. Manage.*, 2025, **373**, 123552.
38 S. Chen, Y. Hu, X. Ye, G. Li, G. Yu, C. Xue and W. Chai, *Biochim. Biophys. Acta, Gen. Subj.*, 2012, **1820**, 989–1000.
39 Q. Xin, Q. Wang, K. Luo, Z. Lei, E. Hu, H. Wang and H. Wang, *Carbohydr. Polym.*, 2024, **324**, 121576.
40 Y. Wen, C. Xue, D. Ji, Y. Hou, K. Li and Y. Li, *Colloids Surf., A*, 2023, **656**, 130531.
41 S. Wang, K. Yao, Z. He, B. Shao, J. Shen and H. Jiang, *J. Environ. Chem. Eng.*, 2023, **11**, 109188.
42 L. Su, S. Wu, W. Zhu, B. Liang, X. Zhang and J. Yang, *J. Environ. Manage.*, 2024, **370**, 122870.
43 S. Shahmoradi, M. Mirshafiei, I. Zare, M. Koohkhezri, H. M. Gholipour, F. Yazdian and E. Mostafavi, Two-Dimensional Nanomater. *Polym. Nanocomposites Process. Prop. Appl.*, 2024, pp. 609–648.
44 X. Ren, Z. Liu, T. Zhang, X. Jiang, Q. Fang, Y. Li, F. Ma, R. Chen, H. Zhang and H. Ni, *J. Mater. Sci.*, 2024, **59**, 10724–10743.
45 M. Al-Shaeli, O. O. Teber, R. A. Al-Juboori, A. Khataee, I. Koyuncu and V. Vatanpour, *Sep. Purif. Technol.*, 2024, 127925.
46 C. Wu, L. Xia, W. Feng and Y. Chen, *ChemPlusChem*, 2024, e202300777.
47 Y. Cai, M. Fang, X. Tan, B. Hu and X. Wang, *Sep. Purif. Technol.*, 2024, 127975.
48 P. Gu, S. Liu, X. Cheng, S. Zhang, C. Wu, T. Wen and X. Wang, *Sci. Total Environ.*, 2023, 169533.
49 S. Kim, F. Gholamirad, M. Yu, C. M. Park, A. Jang, M. Jang, N. Taheri-Qazvini and Y. Yoon, *Chem. Eng. J.*, 2021, **406**, 126789.
50 S. Adil and J.-O. Kim, *Sep. Purif. Technol.*, 2023, **326**, 124725.
51 A. A. Ghani, A. Shahzad, M. Moztahida, K. Tahir, H. Jeon, B. Kim and D. S. Lee, *Chem. Eng. J.*, 2021, **421**, 127780.
52 R. Chen, Y. Cheng, P. Wang, Q. Wang, Z. Yang, C. Tang, S. Xiang, S. Luo, S. Huang, C. Su and Y. Wang, *Chem. Eng. J.*, 2021, **421**, 129682.
53 F. Shi, Y. Chang, J. Shen, G. Chen and C. Xue, *Food Hydrocolloids*, 2023, **134**, 108081.
54 L. Xing, H. Cheng, Y. Li, Q. Chen and X. Liu, *Chem. Eng. J.*, 2024, **487**, 150729.
55 E. A. Imam, A. I. Hashem, A. A. Tolba, M. G. Mahfouz, I. E.-T. El-Sayed, A. I. El-Tantawy, A. A. Galhoum and E. Guibal, *J. Environ. Chem. Eng.*, 2023, **11**, 109951.
56 X. Su, X. Wang, Z. Ge, Z. Bao, L. Lin, Y. Chen, W. Dai, Y. Sun, H. Yuan and W. Yang, *Chem. Eng. J.*, 2024, **486**, 150387.
57 Y. Liu, R. Tian, S. Zhang, T. Bo, Z. Wang, J. Zhao, Y. Wang, G. Lisak, Y. Liu and M. Chang, *Chem. Eng. J.*, 2024, **481**, 148388.
58 X. Huang, P. Zeng, Y. Lu, J. Yang, M. Chen, H. Liu and X. Wang, *Chem. Eng. J.*, 2024, **487**, 150490.
59 X.-M. Cao, J.-Q. Chen, X.-R. Zhao, H. Ge, D. Liu, Q. Wu, Z.-J. Sun and Q. Zhang, *Chem. Eng. J.*, 2024, **479**, 147663.
60 C. Zhang, C. Ma, W. Zhang, Y. Wang, Z. U. Rehman, X. Shen and S. Yao, *Chem. Eng. J.*, 2024, **481**, 148374.
61 M. Wang and X. You, *Chem. Eng. J.*, 2023, **454**, 140417.
62 I. Ijaz, A. Bukhari, A. Nazir, E. Gilani, H. Zain, A. Shaheen, M. R. Shaik and M. Khan, *Sep. Purif. Technol.*, 2025, 131591.
63 Y. Liu, C. Gao, Y. Sun, X. Hao, Z. Pi, M. Yang, X. Zhao and K. Cai, *Chem. Eng. J.*, 2024, 151535.
64 M. A. Islam, D. W. Morton, B. B. Johnson and M. J. Angove, *Sep. Purif. Technol.*, 2020, **247**, 116949.
65 P. Sarker, X. Lei, K. Taylor, W. Holmes, H. Yan, D. Cao, M. E. Zappi and D. D. Gang, *Chem. Eng. J.*, 2023, **454**, 140082.
66 I. Ijaz, A. Bukhari, E. Gilani, A. Nazir, H. Zain, A. Shaheen, M. R. Shaik, M. Khan and M. E. Assal, *Int. J. Biol. Macromol.*, 2024, 132690.
67 Y. Xue, M. Kamali, T. M. Aminabhavi, L. Appels and R. Dewil, *Chem. Eng. J.*, 2024, 152037.
68 L. Singh, P. Rekha and S. Chand, *Sep. Purif. Technol.*, 2016, **170**, 321–336.
69 L. Han, Y. Peng, J. Ma, Z. Shi and Q. Jia, *Sep. Purif. Technol.*, 2022, **285**, 120378.
70 Y. Wu, B. Li, X. Wang, S. Yu, Y. Liu, H. Pang, H. Wang, J. Chen and X. Wang, *Chem. Eng. J.*, 2019, **365**, 249–258.
71 Y. Xie, Q. Rong, C. Wen, X. Liu, M. Hao, Z. Chen, H. Yang, G. I. N. Waterhouse, S. Ma and X. Wang, *CCS Chem.*, 2024, **6**, 1908–1919.
72 Y. Ma, C. Zeng, Y. Ding, J. Tang, O. Mašek, Z. Deng, R. Mu and Z. Zhang, *Sep. Purif. Technol.*, 2024, **331**, 125584.
73 C. Yan, J. Li, Z. Sun, X. Wang and S. Xia, *Sep. Purif. Technol.*, 2024, 127457.
74 B. Luo, G. Huang, Y. Yao, C. An, P. Zhang and K. Zhao, *J. Cleaner Prod.*, 2021, **319**, 128692.
75 S. Gul, S. Hussain, H. Khan, M. Arshad, J. R. Khan and A. de Jesus Motheo, *Chemosphere*, 2024, **357**, 141868.
76 H. Cai, M. Rong, Q. Meng, Z. Liu, Y. Zhao, C. Chen and L. Yang, *Sep. Purif. Technol.*, 2024, **331**, 125612.
77 Y. Chen, Y. Liu, Y. Li, L. Zhao, Y. Chen, H. Li, Y. Liu, L. Li, F. Xu and M. Li, *Environ. Sci. Pollut. Res.*, 2020, **27**, 38644–38653.

78 A. Bukhari, I. Ijaz, E. Gilani, A. Nazir, H. Zain, S. Muhammad, A. Bukhari and S. Hussain, *Chem. Eng. J.*, 2023, **474**, 145890.
79 Q. Zhao, X. Zhu and B. Chen, *Chem. Eng. J.*, 2018, **334**, 1119–1127.
80 M. Zhang, H. Hao, C. Shi, C. Chen, G. Zhou, J. Wang, Y. Cao and X. Han, *Sep. Purif. Technol.*, 2023, **310**, 123095.
81 K. Burdzy, Y. Ju and D. Kołodyńska, *Chem. Eng. J.*, 2023, **461**, 142059.
82 Y.-Y. Chen and J.-G. Yu, *J. Environ. Chem. Eng.*, 2022, **10**, 108348.
83 J. Ouyang, J. Chen, S. Ma, X. Xing, L. Zhou, Z. Liu and C. Zhang, *Particuology*, 2022, **62**, 71–78.
84 R. Zhang, X. Zheng, B. Chen, J. Ma, X. Niu, D. Zhang, Z. Lin, M. Fu and S. Zhou, *J. Cleaner Prod.*, 2020, **256**, 120662.
85 L. Chen, M. Wang, Q. Sun, Z. Zhao, J. Han, R. Ji, X. Jiang, Y. Song, J. Xue and H. Cheng, *Sep. Purif. Technol.*, 2024, **333**, 125940.
86 F. An, B. Gao, X. Huang, Y. Zhang, Y. Li, Y. Xu, Z. Zhang, J. Gao and Z. Chen, *React. Funct. Polym.*, 2013, **73**, 60–65.
87 N. Yao, C. Li, J. Yu, Q. Xu, S. Wei, Z. Tian, Z. Yang, W. Yang and J. Shen, *Sep. Purif. Technol.*, 2020, **236**, 116278.
88 Y. Zhou, Y. He, Y. Xiang, S. Meng, X. Liu, J. Yu, J. Yang, J. Zhang, P. Qin and L. Luo, *Sci. Total Environ.*, 2019, **646**, 29–36.
89 N. Li, L. Zhou, X. Jin, G. Owens and Z. Chen, *J. Hazard. Mater.*, 2019, **366**, 563–572.
90 X. Jiang, J. Guo, M. Sun, Q. Sun, W. Ding, H. Li and H. Zheng, *Chem. Eng. J.*, 2024, **486**, 150391.
91 R. Zhao, W. Ding, M. Sun, L. Yang, B. Liu, H. Zheng and H. Li, *Sep. Purif. Technol.*, 2022, **287**, 120487.
92 I. Ijaz, A. Bukhari, E. Gilani, A. Nazir, H. Zain, A. Bukhari, A. Shaheen, S. Hussain and A. Imtiaz, *Process Biochem.*, 2023, **129**, 257–267.
93 Y. Wu, H. Zheng, H. Li, Y. Sun, C. Zhao, R. Zhao and C. Zhang, *Chem. Eng. J.*, 2021, **426**, 127208.
94 T. Zhang, M. Wang, W. Yang, Z. Yang, Y. Wang and Z. Gu, *Ind. Eng. Chem. Res.*, 2014, **53**, 14913–14920.